RESEARCH ARTICLE

Mechanisms of Resistance to Oncogenic KRAS Inhibition in Pancreatic Cancer

Julien Dilly[1,2,3], Megan T. Hoffman[3,4], Laleh Abbassi[1,2,3], Ziyue Li[1,2], Francesca Paradiso[5], Brendan D. Parent[1,2], Connor J. Hennessey[1,2], Alexander C. Jordan[1,2], Micaela Morgado[1], Shatavisha Dasgupta[1], Giselle A. Uribe[1,2], Annan Yang[1,2], Kevin S. Kapner[1,2], Felix P. Hambitzer[4], Li Qiang[3,4], Hanrong Feng[1], Jacob Geisberg[6], Junning Wang[1], Kyle E. Evans[1,2,3], Hengyu Lyu[7], Aislyn Schalck[7], Ningping Feng[7], Anastasia M. Lopez[7], Christopher A. Bristow[7], Michael P. Kim[7], Kimal I. Rajapakshe[5], Vahid Bahrambeigi[5], Jennifer A. Roth[2], Kavita Garg[8], Paola A. Guerrero[5], Ben Z. Stanger[9], Simona Cristea[2,6,10], Scott W. Lowe[11], Timour Baslan[9], Eliezer M. Van Allen[1], Joseph D. Mancias[3,12], Emily Chan[13], Abraham Anderson[13], Yuliya V. Katlinskaya[13], Alex K. Shalek[2,14,15], David S. Hong[16], Shubham Pant[16], Jill Hallin[17], Kenna Anderes[17], Peter Olson[17], Timothy P. Heffernan[7], Seema Chugh[1,2,3], James G. Christensen[17], Anirban Maitra[5], Brian M. Wolpin[1,3,18], Srivatsan Raghavan[1,2,3,18], Jonathan A. Nowak[18,19], Peter S. Winter[2], Stephanie K. Dougan[3,4], and Andrew J. Aguirre[1,2,3,18]

ABSTRACT KRAS inhibitors demonstrate clinical efficacy in pancreatic ductal adenocarcinoma (PDAC); however, resistance is common. Among patients with *KRAS*^{G12C}-mutant PDAC treated with adagrasib or sotorasib, mutations in *PIK3CA* and *KRAS*, and amplifications of *KRAS*^{G12C}, *MYC*, *MET*, *EGFR*, and *CDK6* emerged at acquired resistance. In PDAC cell lines and organoid models treated with the KRAS^{G12D} inhibitor MRTX1133, epithelial-to-mesenchymal transition and PI3K-AKT-mTOR signaling associate with resistance to therapy. MRTX1133 treatment of the *Kras*$^{LSL\text{-}G12D/+}$; *Trp53*$^{LSL\text{-}R172H/+}$; p48-*Cre* (KPC) mouse model yielded deep tumor regressions, but drug resistance ultimately emerged, accompanied by amplifications of *Kras*, *Yap1*, *Myc*, *Cdk6, and Abcb1a/b*, and co-evolution of drug-resistant transcriptional programs. Moreover, in KPC and PDX models, mesenchymal and basal-like cell states displayed increased response to KRAS inhibition compared to the classical state. Combination treatment with KRAS^{G12D} inhibition and chemotherapy significantly improved tumor control in PDAC mouse models. Collectively, these data elucidate co-evolving resistance mechanisms to KRAS inhibition and support multiple combination therapy strategies.

SIGNIFICANCE: Acquired resistance may limit the impact of KRAS inhibition in patients with PDAC. Using clinical samples and multiple preclinical models, we define heterogeneous genetic and nongenetic mechanisms of resistance to KRAS inhibition that may guide combination therapy approaches to improve the efficacy and durability of these promising therapies for patients.

See related commentary by Marasco and Misale, p. 2018

INTRODUCTION

Pancreatic ductal adenocarcinoma (PDAC) is a devastating disease. Most patients present with advanced cancer and die within 12 months of diagnosis due to limited therapeutic options and poor responses to standard-of-care chemotherapy (1, 2). *KRAS* is the dominant oncogene in PDAC and is altered in more than 90% of tumors, with G12D, G12V, and G12R substitutions being most frequently observed (3, 4). Oncogenic *KRAS* mutations typically increase the steady-state levels of the protein in the active GTP-bound form, which drives protumorigenic signaling through downstream effector pathways, such as the mitogen-activated protein kinase (MAPK) and phosphatidylinositol 3-kinase (PI3K) pathways. Prior studies have demonstrated that genetic ablation of KRAS expression leads to cell cycle arrest and death in cell lines and potent tumor regressions in animal models of PDAC (5–7). Thus, KRAS is a well-validated, high-priority therapeutic target for PDAC.

Recent advances in medicinal chemistry have enabled the development of direct small-molecule inhibitors of KRAS, including covalent inhibitors of the KRAS^{G12C} protein that impair oncogenic signaling and cause tumor regressions in preclinical models (8–10). Clinical trials of multiple KRAS^{G12C} inhibitors have shown promising efficacy in advanced, previously treated non–small cell lung cancer (NSCLC), leading to United States Food and Drug Administration (FDA) accelerated approval of two of these therapies (adagrasib and sotorasib) and many others being investigated in this setting (9–17). We and others have recently described mechanisms of acquired resistance in patients with lung and colorectal

[1]Department of Medical Oncology, Dana-Farber Cancer Institute, Boston, Massachusetts. [2]The Broad Institute of Harvard and MIT, Cambridge, Massachusetts. [3]Harvard Medical School, Boston, Massachusetts. [4]Department of Cancer Immunology and Virology, Dana-Farber Cancer Institute, Boston, Massachusetts. [5]Department of Translational Molecular Pathology, Sheikh Ahmed Center for Pancreatic Cancer Research, The University of Texas MD Anderson Cancer Center, Houston, Texas. [6]Department of Data Science, Dana-Farber Cancer Institute, Boston, Massachusetts. [7]Therapeutics Discovery Division, TRACTION Platform, The University of Texas MD Anderson Cancer Center, Houston, Texas. [8]Exact Sciences, Redwood City, California. [9]Department of Medicine, Perelman School of Medicine, University of Pennsylvania, Philadelphia, Pennsylvania. [10]Harvard School of Public Health, Boston, Massachusetts. [11]Cancer Biology and Genetics Program, Memorial Sloan Kettering Cancer Center, New York, New York. [12]Department of Radiation Oncology, Dana-Farber Cancer Institute, Boston, Massachusetts. [13]Amgen Inc., Thousand Oaks, California. [14]Ragon Institute of MGH, MIT, and Harvard, Cambridge, Massachusetts. [15]Institute for Medical Engineering and Science, Department of Chemistry, and Koch Institute for Integrative Cancer Research, Massachusetts Institute of Technology, Cambridge, Massachusetts. [16]University of Texas M.D. Anderson Cancer Center, Houston, Texas. [17]Mirati Therapeutics Inc., San Diego, California. [18]Department of Medicine, Brigham and Women's Hospital, Boston, Massachusetts. [19]Department of Pathology, Brigham and Women's Hospital, Boston, Massachusetts.

J. Dilly, M.T. Hoffmann, L. Abbassi, Z. Li, and F. Paradiso contributed equally to this article.

S. Raghavan, J.A. Nowak, P.S. Winter, S.K. Dougan, and A.J. Aguirre are co-senior authors of this article.

Corresponding Author: Andrew J. Aguirre, Dana-Farber Cancer Institute, 450 Brookline Avenue, Boston, MA 02215. E-mail: andrew_aguirre@dfci.harvard.edu

Cancer Discov 2024;14:2135–61

doi: 10.1158/2159-8290.CD-24-0177

cancer (CRC) treated with KRAS^{G12C} inhibitors, including mutations in *KRAS* or other RTK–RAS–MAPK pathway effectors, adaptive signaling alterations, and histologic transformation to drug-resistant cell states (14, 18–24). Circulating tumor DNA (ctDNA) samples from patients in these studies revealed a complex landscape of acquired resistance, with emergence of multiple putative genetic drivers of resistance within subsets of patients. Despite these early findings, there remains a critical need for an improved understanding of mechanisms of response and resistance to KRAS inhibitors in each relevant cancer type to guide the effective use of these therapies and improve clinical outcomes for patients.

KRAS^{G12C} mutations are rare in PDAC (~1.5% of patients; ref. 25); however, early clinical results using KRAS^{G12C} inhibitors in patients with PDAC are promising. The CodeBreaK100 (NCT03600883) clinical trial evaluated the safety and efficacy of sotorasib in advanced KRAS^{G12C}-mutant cancers, including 38 patients with metastatic, previously chemotherapy-treated PDAC. In these patients, a 21% objective response rate (ORR), a median progression-free survival (PFS) of 4.0 months, and a median overall survival (OS) of 6.9 months were observed (26). The KRYSTAL-1 (NCT03785249) study included 21 advanced, previously treated patients with KRAS^{G12C}-mutant PDAC who received adagrasib monotherapy. In this cohort, an ORR of 33.3%, a PFS of 5.4 months, and an OS of 8.0 months were observed (27). Although these early clinical trial results need to be confirmed in larger studies, the efficacy of sotorasib and adagrasib in advanced, chemotherapy-treated disease compares favorably to historical data on second-line chemotherapy efficacy in PDAC, where response rates are consistently less than 10% and median PFS is less than 3 months (28, 29). While these results suggest that direct KRAS inhibition can confer substantial clinical benefit, responses are of limited duration, and essentially all patients with PDAC treated with KRAS^{G12C} inhibitors have developed progressive disease (PD) on therapy, with mechanisms of resistance not yet fully elucidated.

KRAS^{G12D} mutations occur in nearly 40% of PDAC (25) and the recent development of selective inhibitors of the KRAS^{G12D} mutant protein may have substantial clinical impact on the treatment of patients with PDAC (30, 31). MRTX1133 is a potent, selective, and non-covalent KRAS^{G12D} inhibitor that has been shown to preferentially target the inactive, GDP-bound form of the mutant protein with >1,000-fold selectivity over wild-type (WT) KRAS. Recent preclinical work with MRTX1133 has demonstrated excellent responses in cell line and xenograft models of PDAC (30, 32). Moreover, MRTX1133 has been shown to confer robust short-term responses in genetically engineered mouse models (GEMM) of PDAC (33) and displayed increased efficacy when combined with immune checkpoint blockade (32). Additional investigations of combination therapy strategies with MRTX1133 in preclinical models of PDAC have suggested that co-targeting of EGFR may have enhanced efficacy over monotherapy (30, 34). Given the strong preclinical data, MRTX1133 is currently being examined in a multicenter, first-in-human phase 1/2 clinical trial (NCT05737706).

Mechanisms of acquired or primary resistance to KRAS inhibitors in PDAC remain poorly understood. Prior studies using inducible suppression of KRAS via RNA interference or genetically engineered inducible *Kras*^{G12D} alleles (i.e., "*iKras*" model) have suggested that amplification of *YAP1* or induction of an epithelial-to-mesenchymal transition (EMT) can confer a state of RAS independence and overcome KRAS^{G12D} suppression (35–38). Furthermore, studies of the *iKras* mouse model have highlighted myriad mechanisms to enable bypass of oncogenic KRAS addiction, including the adoption of a KRAS-independent cell state dependent on oxidative phosphorylation (5), induction of SMARCB–MYC-network-driven mesenchymal reprogramming (38), activation of the TGFβ-SMAD3/4 axis via TME remodeling (39), and USP21-mediated upregulation of macropinocytosis (40). While these studies of the *iKras* mouse model have identified important potential mechanisms of resistance to oncogenic KRAS extinction, the advent of mutant-selective inhibitors of KRAS now affords an unprecedented opportunity to fully interrogate the molecular basis for response and resistance to this class of therapeutics in a wide array of preclinical PDAC model systems, in addition to patient samples from early phase clinical trials.

Here, we present a multimodal characterization of response and resistance to mutant-selective KRAS inhibition in patients with PDAC treated with the KRAS^{G12C} inhibitors adagrasib or sotorasib, as well as in multiple *in vitro* and *in vivo* models using the KRAS^{G12D} inhibitor MRTX1133. We identified multiple putative genetic mechanisms of resistance in patients as well as heterogeneous genetic and non-genetic resistance mechanisms in preclinical models. These studies define key aspects of the biology of response and resistance to KRAS inhibition in PDAC and may guide the development of combination therapy strategies.

RESULTS

Genetic Mechanisms of Resistance to KRAS^{G12C} Inhibition in Patients with PDAC

To understand mechanisms of resistance to mutant-selective KRAS inhibition in PDAC, we sequenced ctDNA from pretreatment (PT) and post-progression [end of therapy (EOT)] plasma samples obtained from a rare cohort of patients with KRAS^{G12C}-mutant PDAC treated with KRAS^{G12C} inhibitors, including patients who demonstrated resistance to adagrasib monotherapy on the KRYSTAL-1 trial (patients 1–8) or to sotorasib monotherapy on the CodeBreaK100 trial (patients 9–22; Fig. 1; Supplementary Fig. S1; Supplementary Table S1; "Methods"). Partial response (PR) or stable disease (SD) was observed in 18/22 (81%) patients with PDAC from this cohort, all of whom developed acquired resistance to therapy. Primary resistance with PD was observed in 4/22 patients (patients 1, 9, 10, 11). The KRAS^{G12C} allele was detectable in most PT (21/22) and EOT (20/22) samples sequenced using an NGS panel and/or via droplet digital PCR (ddPCR) assay (Fig. 1A and C; Supplementary Fig. S1A). Putative genetic mechanisms of primary or acquired resistance were identified in 9/22 (41%) patients (Fig. 1A–C). In 3/4 patients displaying PD, putative mechanisms of resistance included high-level amplifications of *MYC* (patient 1), concomitant gains/amplification of *KRAS*^{G12C}, *BRAF*, *ERBB2*, *CDK4* (patient 9), and an increased variant allele frequency (VAF)

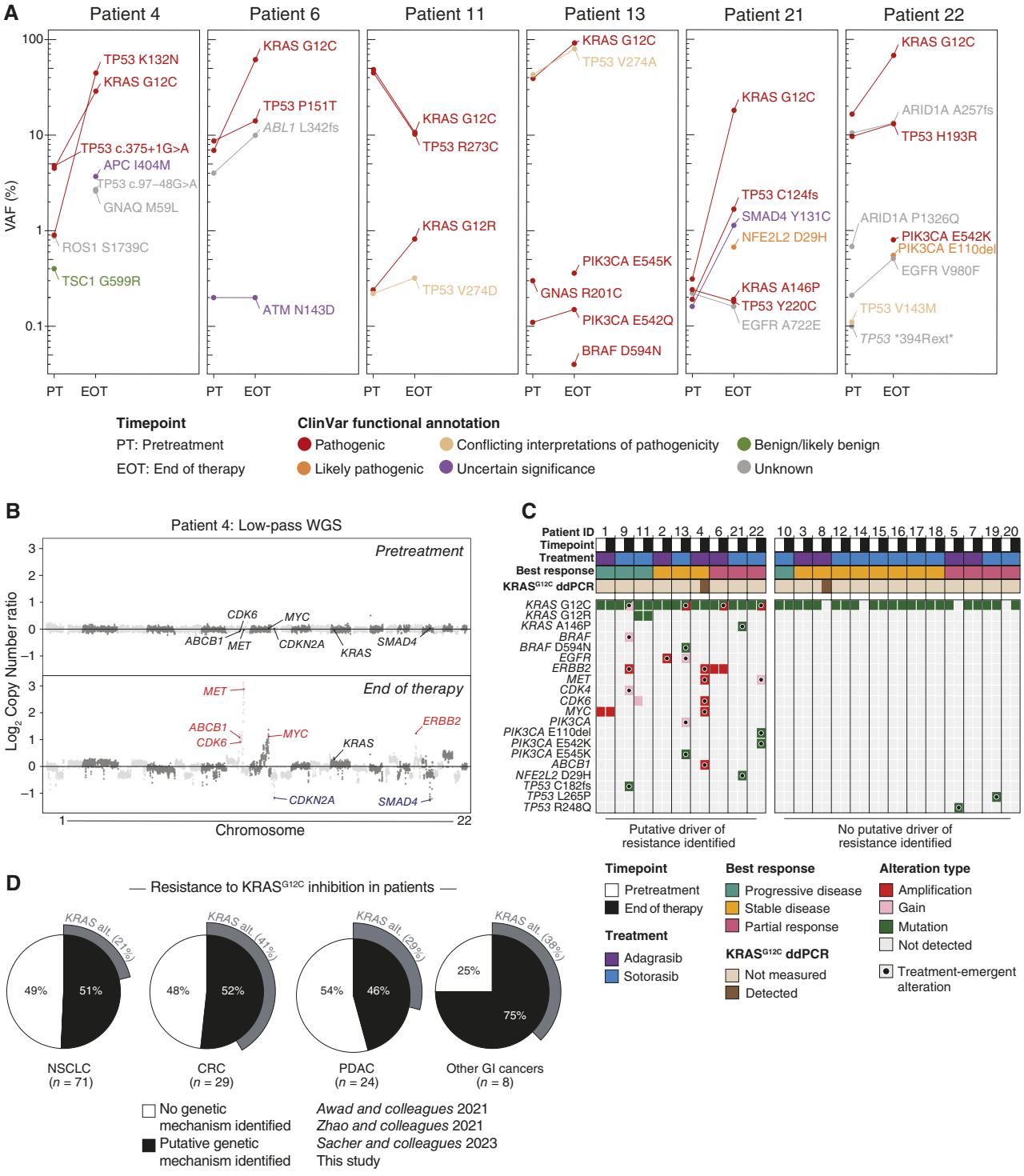

Figure 1. Genetic alterations associated with acquired resistance to KRAS^{G12C} inhibition in patients with PDAC. **A,** Variant allele frequencies (VAF) for the indicated genomic variants in pretreatment (PT) and end of therapy (EOT) ctDNA samples across patients with PDAC treated with adagrasib monotherapy on the KRYSTAL-1 trial (patients 4, 6) or sotorasib monotherapy on the CodeBreaK100 trial (patients 11, 13, 21, 22). **B,** Paired genome-wide copy number profiles from low-pass whole genome sequencing (organized by chromosome and genomic coordinates) from PT and EOT ctDNA samples for patient 4 treated with adagrasib. Gene labels indicate amplified putative drivers of acquired resistance or tumor suppressor genes. **C,** Co-mutation plot displaying pathogenic and likely pathogenic treatment-emergent variants and genomic amplification of putative drivers of resistance detected in ctDNA samples from PDAC patients with acquired resistance to adagrasib (patients 1–8) or sotorasib (patients 9–22). The best radiographic treatment response is indicated as measured by RECIST criteria. **D,** Aggregated classification of mechanisms of resistance to KRAS^{G12C} inhibition across cancer types. Data include patients from this study and previously published studies (Supplementary Table S2; Supplementary Fig. S1G).

of a preexisting, subclonal KRAS^{G12R} variant (patient 11). Treatment-emergent alterations at the time of acquired resistance were observed in several patients, including amplifications/gains of *KRAS*^{G12C} (patients 6, 9, 13, 22), amplification/gain of *EGFR* (patients 2, 13), activating *PIK3CA* mutations (patients 13, 22), and an oncogenic NFE2L2^{D29H} variant (patient 21; Fig. 1C; Supplementary Fig. S1A and S1B). In patient 4, we detected multiple treatment-emergent alterations in the EOT sample via low-pass whole genome sequencing (WGS) of cell-free DNA, including high-level amplifications of *ERBB2*, *MET*, *CDK6*, *MYC*, and *ABCB1* (Fig. 1B and C). While drug-binding site mutations have been previously reported to occur in subsets of patients with NSCLC or CRC experiencing progression on KRAS^{G12C} inhibitors (14, 18), we did not observe any in our PDAC cohort. However, we identified a single treatment–emergent KRAS^{A146P} mutation at EOT (patient 21; Fig. 1A and C). This mutation was previously identified to confer resistance to both sotorasib and an analog of adagrasib when occurring in *cis* with the G12C mutation (18).

In patients 4 and 8, we performed serial collection of plasma throughout the patients' clinical course of response and resistance to adagrasib. During the early phase of treatment, we observed a reduction in the circulating tumor marker CA19-9 and a corresponding reduction of radiographic tumor burden in both patients, as measured by the sum of longest diameters (SLD) of the target lesions [Supplementary Fig. S1C (top)]. At acquired resistance and progression, we detected a rise in CA19-9 accompanied an increase in SLD. We additionally conducted transcriptome analysis of plasma extracellular vesicle RNA (evRNA; ref. 41) as a pharmacodynamic biomarker in one patient who initially responded to therapy (patient 4), and we observed reduced KRAS pathway activity at the transcriptional level during response and a corresponding increase at the time of progression, suggesting pathway reactivation at resistance in this patient [Supplementary Fig. 1C (bottom)].

To better define the landscape of putative genetic mechanisms of acquired resistance to KRAS^{G12C} inhibition across different cancer types, we integrated data from the 22 patients with PDAC in our cohort (Fig. 1A–C), along with four additional new paired PT and EOT ctDNA profiles from patients with other GI malignancies (Supplementary Fig. S1D–S1F), and previously published results from ctDNA profiling of acquired resistance to adagrasib, sotorasib, or divarasib across multiple tumor types (Supplementary Fig. S1G; Supplementary Table S2; "Methods"; refs. 14, 18, 19). In this aggregate cohort of patients, putative genetic mechanisms of resistance were identified by ctDNA in 51% of NSCLC, 52% of CRC, 46% of PDAC, and 75% of other GI cancers (Fig. 1D). Treatment-emergent *KRAS* alterations, including point mutations and copy number amplifications, were observed in 41% of patients with CRC; however, they were less frequent in NSCLC (21%) and PDAC (29%). Importantly, in large subsets of patients with PDAC (54%), NSCLC (49%), or CRC (48%), a putative genetic mechanism of resistance could not be identified, suggesting either incomplete detection of treatment-emergent genetic drivers of resistance by ctDNA-based approaches, and/or a strong contribution of non-genetic mechanisms in mediating acquired resistance to KRAS^{G12C} inhibition across cancer types.

Biomarkers of Response and Resistance to KRAS^{G12D} Inhibition in PDAC

The KRAS^{G12C} mutation is rare in PDAC and very few KRAS^{G12C}-mutant patient-derived PDAC models have been developed. Therefore, we sought to define potential biomarkers of response and resistance to mutant-selective KRAS inhibition more broadly by investigating *in vitro* sensitivity to the KRAS^{G12D} inhibitor MRTX1133 via a PRISM multiplex pooled screening assay across 877 human cancer cell lines from different genetic and histological backgrounds ("Methods"; refs. 42, 43). We observed significant and selective antiproliferative activity of MRTX1133 for KRAS^{G12D}-mutated cell lines in comparison to KRAS^{WT} cell lines or those harboring other KRAS alterations (Fig. 2A; Supplementary Table S3). While we did not observe lineage-specific sensitivity to MRTX1133 across KRAS^{G12D} mutated cell lines in the PRISM cohort (n = 46; Supplementary Fig. S2A), we observed a bimodal distribution of cell lines within this group, as measured by the area under the dose-response curve (AUC), irrespective of the lineage. We then classified cell lines as "sensitive" (n = 22) or "resistant" (n = 24) based on their AUC for MRTX1133 (Fig. 2B; Supplementary Fig. S2A, "Methods").

We next examined biomarkers associated with either sensitivity or resistance to MRTX1133 across KRAS^{G12D}-mutated PDAC cell lines (n = 16; Fig. 2B). Notably, we did not observe significant variation in response to MRTX1133 based on the presence of alterations in frequently co-mutated tumor suppressor genes (i.e., *TP53*, *CDKN2A*, *SMAD4*, *ARID1A*; Supplementary Fig. S2B). We next interrogated gene copy number (CN), bulk RNA sequencing (RNA-seq), and reverse phase protein array (RPPA) datasets for feature distinctions between sensitive and resistant PDAC cell lines (Fig. 2C; Supplementary Tables S4A and S4B). In the resistant lines compared with the sensitive subset, we observed relative CN elevations of RTK–RAS pathway genes (*EGFR*, *MET*, *BRAF*, *ETV1*), as well as EMT regulators (*ZEB1*, *TWIST1*; Fig. 2D; Supplementary Fig. S2C). At the transcriptional level, gene set enrichment analysis (GSEA) identified upregulation of signatures related to EMT, cell-cycle progression, and MYC activity in MRTX1133-resistant cell lines compared with the sensitive subset (Fig. 2E; Supplementary Fig. S2D). We did not observe stratification of the response to MRTX1133 based on cell state identity along the basal-like/classical axis using *in vitro* PDAC cell line models (Supplementary Fig. S2E). Notably, cell line models in standard two-dimensional culture conditions have previously been shown to demonstrate baseline bias toward the basal-like state, thus making basal-like versus classical comparisons of MRTX1133 sensitivity challenging (44). Moreover, sensitive cell lines were characterized by a relative upregulation of KRAS activity at the transcriptional level (Fig. 2E). At the protein level, RPPA data showed higher levels of effector proteins from the PI3K–AKT–mTOR signaling pathway (including PI3K-p85α and p110α subunits, mTOR, Rictor, pS6 S235/S236), elevated expression of translation regulators (eIF4G, eEf2K), and increased total and phosphorylated (pS445) BRAF protein levels in resistant lines, along with higher expression of E-Cadherin and β-catenin in MRTX1133-sensitive cell lines (Fig. 2F).

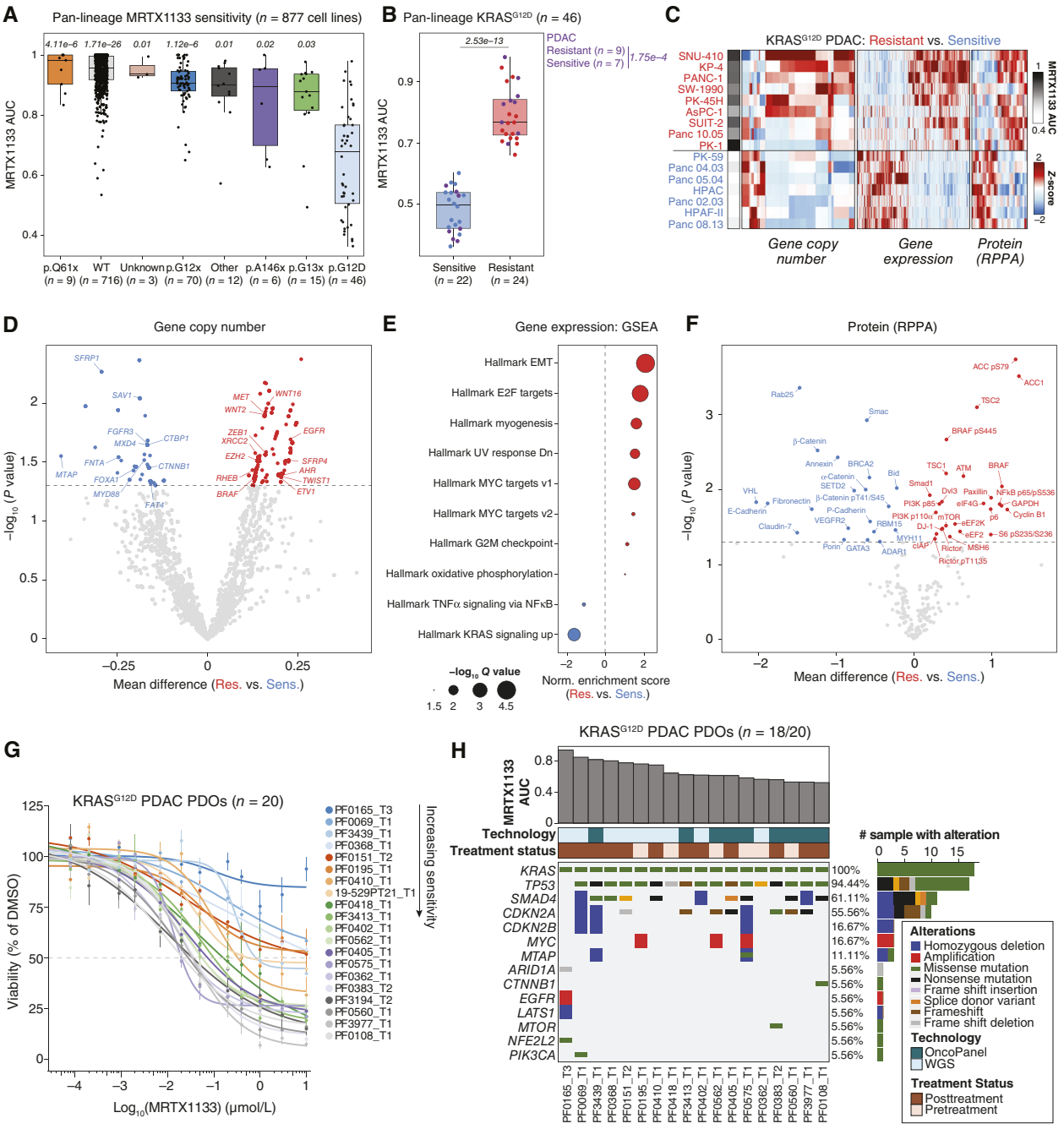

Figure 2. Multiomic analysis identifies baseline features of response and resistance to KRAS^{G12D} inhibition. **A,** Boxplot representing the response to MRTX1133 plotted as the area under the dose-response curve (AUC) for 877 cell lines evaluated in the PRISM multiplex cell line screening assay. Cell lines are grouped by *KRAS* genotypes. AUCs were compared between each *KRAS* genotype relative to *KRAS*^{G12D}. Significance was determined via Kruskal–Wallis test followed by Dunn's test and adjusted with Benjamini–Hochberg correction. The adjusted *P* value for each comparison is displayed on top of each group. **B,** Boxplot depicting the difference in response to MRTX1133 between subsets of resistant and sensitive KRAS^{G12D} cell lines. PDAC cell lines are colored in purple. Significance for the AUC comparison between resistant and sensitive subsets was determined by a two-sided Wilcoxon rank-sum test. **C,** Heatmap depicting differentially expressed features (gene copy number, gene expression, and protein levels) between MRTX1133-resistant and -sensitive KRAS^{G12D} PDAC cell lines. Each column represents a feature that is *Z*-scored across cell lines (rows). **D,** Volcano plot depicting differential gene copy number analysis between resistant and sensitive KRAS^{G12D} PDAC cell lines. The *X*-axis depicts the mean difference of Log_2 copy number ratio calls of each protein-coding gene (relative to ploidy), between resistant and sensitive cell lines. Significance determined by two-sided Student *t* test. **E,** Hallmark transcriptional gene sets significantly enriched or depleted between resistant and sensitive KRAS^{G12D} PDAC cell lines. The normalized enrichment score from GSEA is shown on the *x*-axis. **F,** Volcano plot depicting differentially expressed proteins or phosphorylated proteins between resistant and sensitive KRAS^{G12D} PDAC cell lines. RPPA data were obtained from the Cancer Dependency Map. Significance determined by two-sided Student *t* test. **G,** MRTX1133 dose-response curves for a 6-day cell-titer-glo 3D assays with KRAS^{G12D}-mutant PDAC PDOs. PDO labels are in order of sensitivity, with lower AUC being more sensitive. Points are the mean ± SEM ($n = 3$ biological replicates per PDO). **H,** Co-mutation plot of *KRAS*^{G12D}-mutant PDAC PDOs displaying recurrently altered genes and selected putative drivers of baseline resistance to MRTX1133 across the cohort.

We next performed immunoblotting to validate biomarkers of RAS pathway signaling in epithelial and mesenchymal cell lines with differential sensitivity to MRTX1133 (Supplementary Fig. S2F). While phosphorylated ERK (pERK) levels were variably suppressed upon MRTX1133 treatment across both mesenchymal, resistant cell lines (PANC-1 and KP-4) and epithelial, sensitive cell lines (HPAC and Panc 05.04), mesenchymal cell lines displayed greater PI3K-AKT-mTOR pathway activation at baseline and upon MRTX1133 treatment compared to epithelial cell lines, as indicated by increased levels of phosphorylated-S6 (pS6 S235/S236). Thus, differential PI3K-AKT-mTOR pathway activation may drive baseline resistance to KRAS inhibition *in vitro* in cells displaying features of EMT (Supplementary Fig. S2F).

Response and Resistance to KRAS^{G12D} Inhibition in Patient-Derived Organoid Models

We further characterized the response to MRTX1133 in a panel of early passage patient-derived organoids (PDOs, $n = 20$) developed from KRAS^{G12D}-mutant advanced PDAC tumors representing a range of genotypes and clinical features. We observed a spectrum of responses to MRTX1133 among PDAC PDOs from both treatment-naïve and previously treated cancers, ranging from clear dose-dependent sensitivity in some models to near-complete resistance in others (Fig. 2G; Supplementary Tables S5A and S5B). As previously observed in the PRISM cell line data, response to MRTX1133 in PDOs did not stratify by the presence of alterations in major tumor suppressor genes (Supplementary Fig. S2G). However, we noted multiple other potential resistance mechanisms in the most insensitive PDOs, such as a co-occurring amplification of *EGFR* (Supplementary Fig. S2H) and an oncogenic *NFE2L2*^{D29H} mutation, known to disrupt KEAP1 binding and previously shown to lead to resistance to MAPK-targeted therapies (Fig. 2H; ref. 45). The second most resistant PDO to MRTX1133 (PF0069_T1) harbors a *PIK3CA*^{G118D} mutation, a known oncogenic alteration leading to enhanced PIK3CA activity and signaling (46, 47). Conversely, the PDO exhibiting the greatest sensitivity to MRTX1133 (PF0108_T1) was notable for a *CTNNB1*^{T41A} mutation, a known stabilizing mutation that drives Wnt/β-catenin signaling (Fig. 2H; ref. 48). As previously observed in cell lines, we did not identify a significant stratification of the response to MRTX1133 based on basal-like/classical transcriptional identity in PDO models, although the basal-like cell state is not well represented in PDOs, as previously demonstrated (Supplementary Fig. S2I; ref. 44). Based on the observation in cell lines and PDOs that EGFR and other RTK signaling may drive resistance to KRAS inhibition (Fig. 2D; Supplementary Fig. S2C), we evaluated whether exogenous RTK stimulation could modulate response to MRTX1133 in PDAC PDOs. Removal of EGF and FGF from the standard organoid culture media led to a consistent sensitization of all models examined, further confirming the role of RTK-RAS pathway stimulation in driving baseline resistance to KRAS^{G12D} inhibition (Supplementary Fig. S2J). Collectively, results from PDOs align with data from the PRISM cell line screen and support that activation of RTK-RAS-MAPK and PI3K pathways may drive resistance to mutant-selective KRAS inhibition in PDAC.

Isogenic Cell Culture Models Reveal Diverse Mechanisms of Acquired Resistance

To model acquired resistance to MRTX1133 *in vitro*, we exposed sensitive murine ($n = 3$) and human ($n = 2$) cell line models to dose escalation of MRTX1133 and derived resistant models exhibiting significantly reduced *in vitro* sensitivity to KRAS^{G12D} inhibition when compared to their respective parental cell lines (Fig. 3A and B; Supplementary Fig. S3A–S3C). The resistant lines also showed decreased sensitivity to the MEK inhibitor trametinib but not to gemcitabine, suggesting cross-resistance to other RTK-RAS-MAPK pathway inhibitors but not to chemotherapy. Resistant mouse cell lines, when implanted subcutaneously into C57BL/6 mice, also showed *in vivo* resistance to MRTX1133 (Fig. 3C). We then comprehensively characterized parental and resistant models at the genomic and transcriptional level ($n = 5$ pairs). Using whole exome sequencing (WES), we did not observe any acquired point mutations in *KRAS* or other RTK-RAS-MAPK pathway genes in any of the cell lines characterized (Supplementary Table S6). Furthermore, we observed no copy number alterations (CNA) emerging in resistant human models (Supplementary Fig. S3D). However, in two out of three murine cell lines (6499C4.R and 6419C5.R), we captured high-level gene amplification of *Cdk6* and *Abcb1a*/*Abcb1b* on chromosome 5 at acquired resistance (Fig. 3D), consistent with our observation of a syntenic region amplified in a human PDAC tumor at acquired resistance to adagrasib (patient 4; Fig. 1B and C), and suggestive of dysregulation of cell cycle progression through CDK6 and potential drug efflux via ABCB1A/B as putative mechanisms of acquired resistance. We additionally observed co-amplification of a distinct region of chromosome 5 harboring *Cdk8* in 6419C5.R along with a low-level gain of chromosome 6, housing *Kras* and *Met*, in 6499C4.R.

At a transcriptional level, the *in vitro* models of acquired resistance demonstrated a significant and recurrent upregulation of EMT processes and cycle progression compared to their matched parental models, similar to that observed in the PRISM data (Figs. 2 and 3E; Supplementary Fig. S3E and S3F). These findings were validated at the protein level with increased expression of mesenchymal markers (ZEB1, VIM) and/or decreased E-Cadherin expression in the resistant models (Fig. 3F). As we previously observed with the MRTX1133-resistant human cell lines KP-4 and PANC-1, both enriched in EMT features and displaying sustained PI3K–AKT–mTOR signaling upon KRAS^{G12D} inhibition (Supplementary Fig. S2F), we also noted generally higher PI3K/mTOR signaling activity both at baseline and upon MRTX1133 treatment in resistant models compared to their respective parental line, as evidenced by increased phosphorylated-(p)AKT and pS6 levels (Fig. 3F; Supplementary Fig. S3G and S3H). MAPK pathway activity, as determined by levels of pERK, was heterogeneous across treatment timepoints and cell lines.

Given the contribution of RTK-dependent signaling in mediating baseline resistance to MRTX1133 in PDOs (Supplementary Fig. S2J), along with sustained PI3K–AKT–mTOR signaling upon KRAS^{G12D} inhibition in models of acquired resistance, we hypothesized that distinct patterns in RTK upregulation may drive differential MRTX1133 sensitivity in the models of acquired resistance. We interrogated

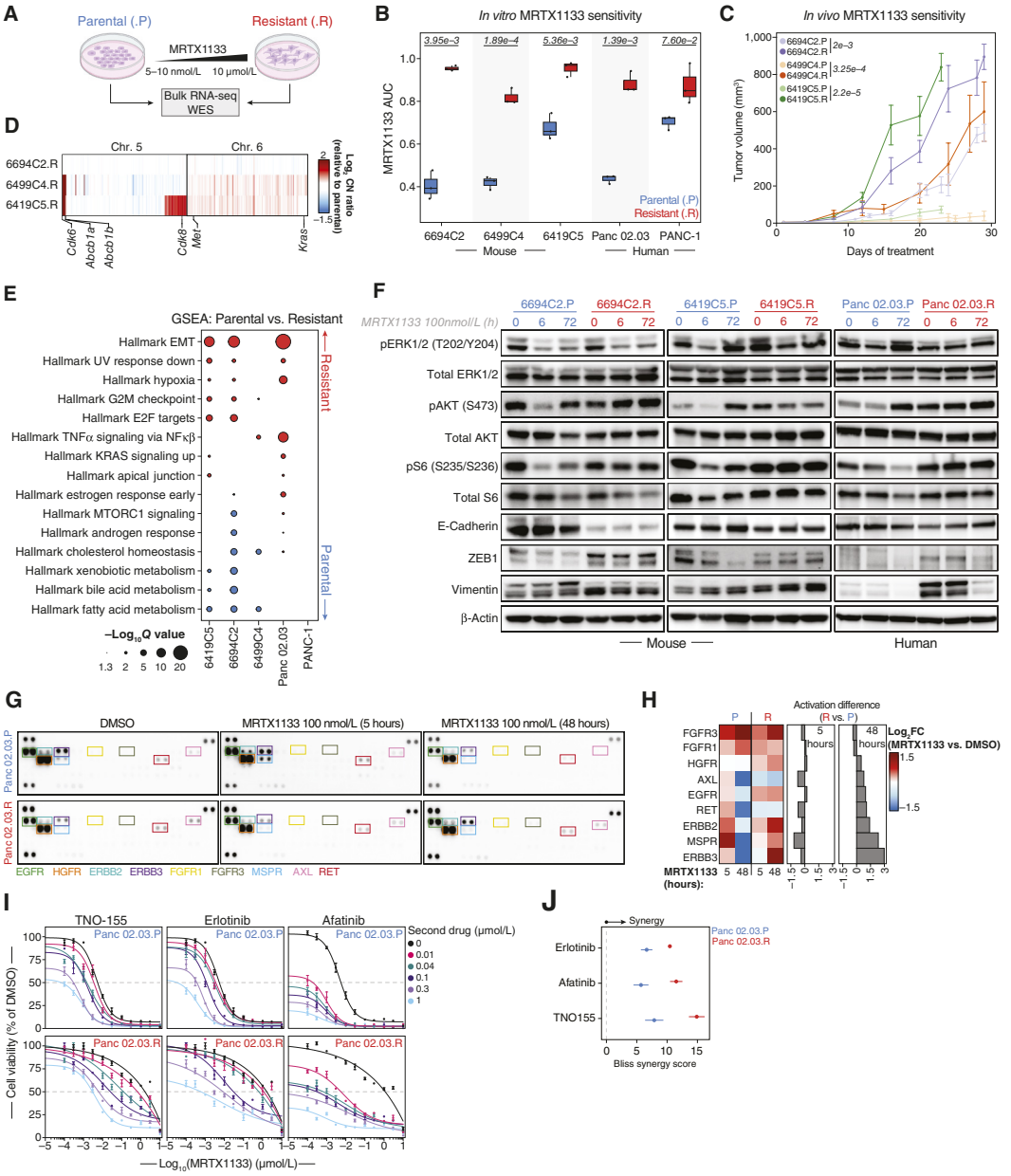

Figure 3. CNAs, EMT, and differential RTK signaling drive acquired resistance to KRAS^{G12D} inhibition *in vitro*. **A,** Experimental workflow used to generate and characterize isogenic models of acquired resistance to MRTX1133. Parental (.P, blue) and resistant (.R, red) cell line labeling is consistent throughout this figure. **B,** Pairwise comparisons of the AUC for MRTX1133 between parental and derived resistant murine and human cell lines. Significance determined by two-sided Student *t* test ($n = 3$ biological replicates per cell line). The *P* value for each comparison is displayed at the top of each cell line pair. **C,** MRTX1133 treatment of syngeneic subcutaneous implant models of parental and resistant murine PDAC cell lines in C57BL6/J mice. Points are the mean ± SEM ($n = 5$ double-flanked mice per cell line). Significance was determined using a two-sided Wilcoxon rank-sum test on AUCs between resistant and parental cell lines. The *P* value for each comparison is displayed next to each cell line pair. **D,** Heatmap of copy number profiles at chromosomes 5 and 6, obtained from DNA WES of murine-resistant cell lines. Copy number ratios are calculated relative to each resistant cell line's matched parental line. Genes are organized by chromosome and genomic coordinates. Amplified/gained putative drivers of resistance to MRTX1133 are labeled. **E,** Hallmark transcriptional gene sets significantly enriched in resistant (red) compared with matched parental (blue) human and murine cell lines. **F,** Immunoblots of murine and human isogenic parental/resistant cell line pairs treated with MRTX1133 (100 nmol/L) for the indicated duration. β-actin was used as protein loading control. **G,** Receptor tyrosine kinase (RTK) arrays of Panc 02.03 parental (.P) and resistant (.R) cell line pair, treated with DMSO or MRTX1133 (100 nmol/L) for the indicated timepoints. RTKs differentially activated across treatment conditions and cell lines are labeled. **H,** Left, Heatmap depicting the densitometric quantification showing RTKs differentially activated upon 5 or 48 hours of MRTX1133 treatment relative to matched DMSO-treated control. Right, bar plots depicting the relative densitometric difference for each RTK upon MRTX1133 treatment for the indicated timepoints between the resistant and the parental cell lines. Quantification is representative of two independent experiments. **I,** Dose-response curves based on 5-day cell-titer-glo 2.0 assays for MRTX1133 combination with RTK targeted therapies with the isogenic parental and resistant Panc 02.03 cell lines. Concentrations of the second drug are displayed on the right. TNO-155, allosteric SHP2 inhibitor; erlotinib, EGFR inhibitor; afatinib, multi-targeted inhibitor of EGFR, ERBB2/HER2, and ERBB4. Points are the mean ± SEM ($n = 3$ biological replicates). **J,** Average Bliss synergy score for combinations of MRTX1133 with RTK-directed therapies across parental and resistant Panc 02.03 cell lines. Points are the mean ± SEM ($n = 3$ biological replicates).

RTK signaling in the Panc 02.03 isogenic resistant model using phosphorylated RTK arrays to characterize the activation state of 50 RTKs upon MRTX1133 treatment (Supplementary Fig. S3I). While we did not observe strong differential RTK activation after 5 hours of MRTX1133 treatment between parental and resistant models, we detected increased activation levels of HGFR, EGFR, RET, AXL, ERBB2, ERBB3, and MSPR (encoded by *MST1R*) in the resistant model compared to its matched parental after 48 hours of MRTX1133 treatment, suggesting that activation of multiple RTKs may contribute to the resistant phenotype (Fig. 3G and H). Additionally, targeting of RTK signaling with small-molecule inhibitors showed synergistic activities across both parental and resistant models, further suggesting that RTK signaling contributes to acquired resistance and represents a tractable therapeutic target in combination with KRAS inhibition (Fig. 3I and J). Collectively, these observations highlight the emergence of heterogeneous genetic and non-genetic mechanisms in models of acquired resistance, including genomic amplifications of cell cycle regulators, as well as EMT and adaptive RTK signaling that co-evolve to drive acquired resistance to $KRAS^{G12D}$ inhibition *in vitro*.

$Kras^{G12D}$ Inhibition Drives Deep and Durable Responses in an Autochthonous Mouse Model of PDAC

After evaluating features of response and resistance to MRTX1133 *in vitro*, we sought to investigate the efficacy of $KRAS^{G12D}$ inhibition in the immunocompetent, autochthonous KPC (*Kras*$^{LSL\text{-}G12D/+}$; *Trp53*$^{LSL\text{-}R172H/+}$; p48-*Cre*) genetically engineered mouse model (GEMM) of PDAC (49). Mice with the KPC genotype were continuously monitored by palpation and ultrasound, and once tumors reached a size of 100 to 300 mm^3, each mouse was randomized to one of the two treatment arms, receiving either vehicle (n = 12) or MRTX1133 (n = 19; Fig. 4A; Supplementary Tables S7A and S7B; Supplementary Fig. S4A–S4C). To evaluate short-term pharmacological effects, four MRTX1133-treated KPC mice ("Early MRTX1133") and three vehicle-treated control mice ("Early vehicle") were sacrificed after receiving six doses of treatment over 3 days. Tumor volume measurements after 3 days of MRTX1133 treatment suggested that these tumors were responding to $Kras^{G12D}$ inhibition at the time of sacrifice [Supplementary Fig. S4D (top)].

The remaining mice were treated with either MRTX1133 ("Endpoint MRTX1133," n = 15) or vehicle control ("Endpoint vehicle," n = 9) until they reached a humane endpoint (Supplementary Fig. S4B and S4C), thus enabling assessment of response and long-term adaptation and resistance to MRTX1133. While vehicle-treated animals succumbed to aggressive tumor growth within 3 to 15 days post-randomization (Fig. 4B and C), MRTX1133 treatment significantly prolonged the overall survival of mice with PDAC, with a median survival of 10.7 weeks for MRTX1133-treated mice compared to 1 week for vehicle-treated animals (P = 2.08 e–6, Log-rank test; Fig. 4B). We observed PRs and moderate tumor volume reductions in 27% (4/15) of mice in the endpoint MRTX1133-treated cohort, with tumors displaying a subsequent period of SD before ultimately progressing on continuous MRTX1133 treatment [Fig. 4C (middle) and D]. Primary resistance was observed in 1/15 animals, with tumor growth kinetics resembling those of the vehicle-treated mice [Fig. 4C (top and middle)]. Complete responses to MRTX1133 were seen in 67% (10/15) of mice, with rapid and complete tumor regression within the first 2 weeks of treatment, as confirmed by the absence of any detectable tumor via ultrasounds [Fig. 4C (bottom) and D; Supplementary Fig. S4B (bottom row)]. In this group, complete and durable remissions were maintained until acquired resistance developed and mice had to be sacrificed at a humane endpoint (Supplementary Table S7A). In one out of two mice which experienced complete and durable regressions of the primary tumors until the animals reached humane endpoints, we observed peritoneal metastases during necropsy, suggesting that acquired resistance can also manifest in distant spread. Thus, $Kras^{G12D}$ inhibition in the KPC mouse model led to robust tumor responses followed by acquired resistance.

Evolution of Heterogeneous Resistance Mechanisms to $Kras^{G12D}$ Inhibition in the KPC GEMM

To define mechanisms of resistance to MRTX1133, we performed multimodal characterization of both vehicle- and MRTX1133-treated tumors, including WES (n = 20), single-nucleus RNA-seq (snRNA-seq, n = 17) and immunohistochemistry (IHC, n = 17; Supplementary Fig. S4D). At the genomic level, we did not observe putative drug-binding site mutations in *Kras*, such as those that have previously been noted to cause resistance to KRAS inhibition in human tumors (14, 18, 20). However, we observed high-level genomic amplifications in 55% (6/11) of tumors derived from endpoint MRTX1133-resistant animals, that were absent from vehicle-treated tumors (Supplementary Fig. S5A). These included two tumors with a focal amplification of *Myc*, two tumors harboring *Kras* amplification, and two tumors with amplification of *Yap1* (Fig. 4E; Supplementary Fig. S5B). We also identified a high-level amplification of the centromeric region of chromosome 5, which harbors *Cdk6* and *Abcb1a*/*Abcb1b* in two MRTX1133-resistant KPC tumors and an amplification of *Cdk6* alone in another tumor (Fig. 4E; Supplementary Fig. S5B), mirroring our observations in isogenic cell line models of acquired resistance to MRTX1133, as well as in patients with acquired resistance to adagrasib or sotorasib monotherapy (Figs. 1B, C, and 3D). Multiple distinct CNAs were detected in a single MRTX1133-resistant tumor, including amplifications of *Kras*, *Cdk6*, *Yap1*, and *Myc* [KPC_4093; Supplementary Fig. S5B (top row)].

To complement our investigation of genetic mechanisms of resistance in KPC mice, we evaluated transcriptional variation by snRNA-seq across early vehicle (n = 3), early MRTX1133-treated tumors (n = 3), as well as at endpoint vehicle (n = 5) and endpoint, MRTX1133-resistant (n = 6) tumors. We captured 68,479 high-quality nuclei from these tumors, revealing five distinct populations after unsupervised clustering and manual examination of expression patterns for established cell type markers: cancer-associated fibroblasts (CAF), tumor-associated macrophages (TAM), endothelial cells (EC), pericytes, and epithelial cells (Fig. 4F; Supplementary Fig. S6A–S6D). Investigation of non-epithelial cell types in our

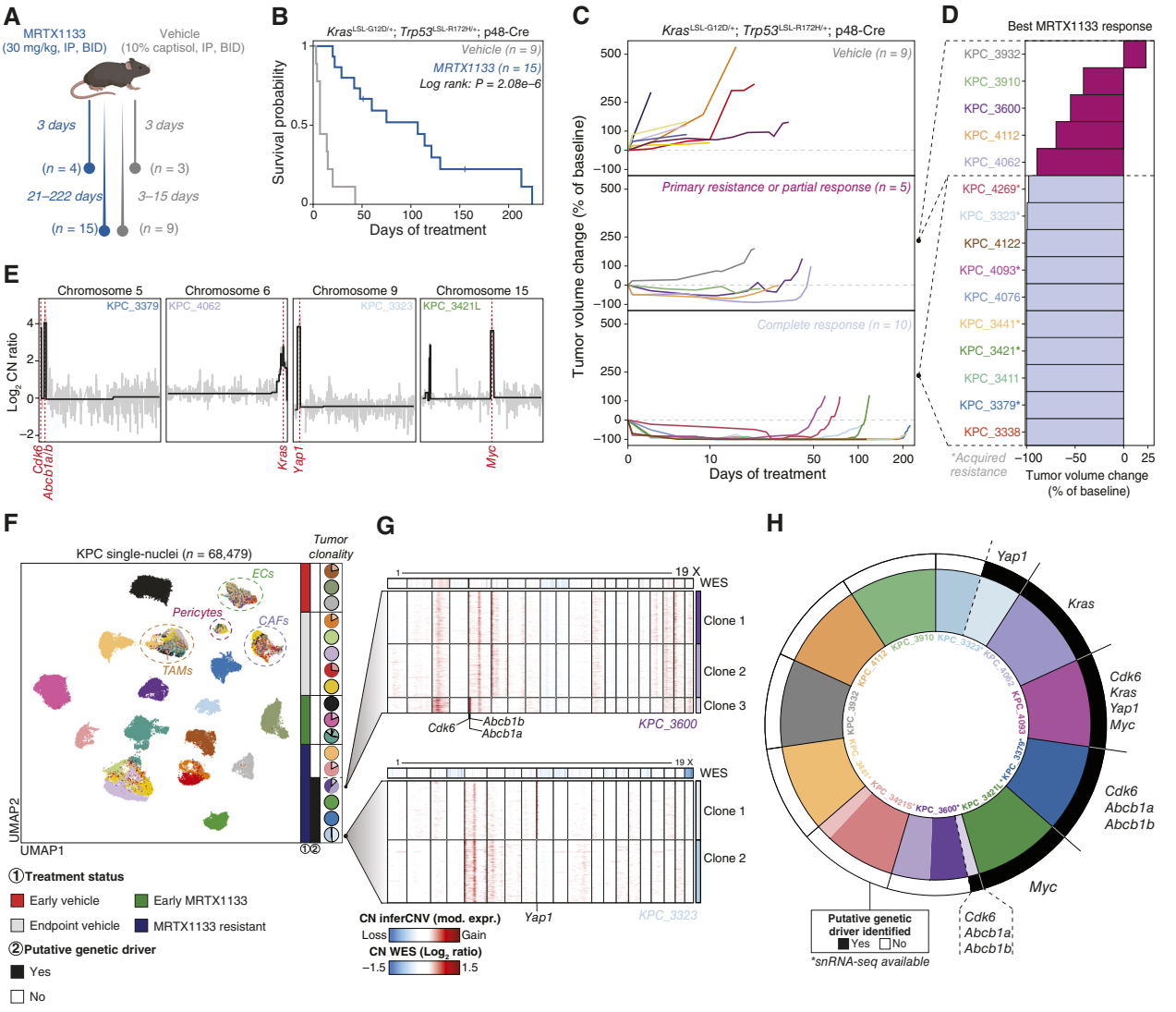

Figure 4. Heterogeneous genomic amplifications drive resistance to KRAS^{G12D} inhibition in the KPC mouse model of PDAC. **A,** Overview of the KPC GEMM treatment study. Early vehicle- and MRTX1133-treated mice were euthanized after 3 days of treatment, and long-term treated endpoint vehicle and MRTX1133-resistant mice were sacrificed at clinical endpoint. **B,** Kaplan–Meier survival curves of KPC mice treated until clinical endpoint with the indicated regimens (Vehicle, $n = 9$; MRTX1133, $n = 15$). **C,** Tumor growth kinetics of KPC mice treated until clinical endpoint, as measured by ultrasound, throughout treatment across the indicated treatment/response groups. **D,** Waterfall plot displaying the maximal tumor response in KPC mice, as measured by the smallest tumor size while on MRTX1133 treatment. **E,** Chromosomal CN profiles from WES demonstrating regions of amplification from MRTX1133-resistant KPC tumors. Genes are displayed by genomic coordinates. The segmented copy number trend is depicted by the black line and amplified putative drivers of resistance to MRTX1133 are labeled in red, with their genomic coordinates indicated by a red line. **F,** Left, UMAP embedding of single-nuclei from KPC PDAC tumors and colored by sample ID. Outlined are the four major non-malignant cell populations identified (CAFs, cancer-associated fibroblasts; ECs, endothelial cells; TAMs, tumor-associated macrophages). Right, Sample-wise pie charts displaying malignant cell clonality as determined by inferCNV. **G,** Heatmaps of single-nucleus CN profiles inferred from snRNA-seq of two MRTX1133-resistant tumors (top: KPC_3600 and bottom: KPC_3323), organized by chromosomes and genomic coordinates (columns). Row splits indicate major subclones identified within each tumor via inferCNV. The top annotation bar indicates the matched genomic reference from WES for the same tumor. Genomic amplifications identified by WES are labeled at the bottom. **H,** Aggregate representation of putative genomic mechanisms of resistance across MRTX1133-resistant KPC tumors. The inner ring indicates tumors and inferred clonality when available/present from snRNA-seq. The outer ring indicates the presence, distribution, and names of the putative genomic drivers of resistance to MRTX1133 identified via WES and inferCNV. * denotes tumors for which snRNA-seq data are available.

snRNA-seq data did not highlight cell populations differentially enriched across treatment groups (Supplementary Fig. S6E–S6I). As we did not detect high-quality lymphocyte populations in the snRNA-seq data, we further characterized tumor infiltrating immune populations via flow cytometry. We did not detect any differentially enriched immune cell populations between endpoint vehicle and MRTX1133-resistant tumors (Supplementary Fig. S6J). Thus, we focused further studies on the malignant cell compartment to describe MRTX1133 response and resistance.

First, we distinguished putative malignant epithelial cells from non-malignant populations in each tumor via inferred CNA scores (Supplementary Fig. S7A). Next, we assessed proximal pathway inhibition by MRTX1133 in malignant

nuclei (n = 58,039) using MAPK pathway transcriptional activity as a pharmacodynamic biomarker for KRAS^{G12D} inhibition. We observed significant suppression of MAPK pathway activity in the MRTX1133-treated tumors compared to vehicle-treated tumors (Supplementary Fig. S7B). We observed a similar decrease in pERK protein levels via IHC in tumors treated with MRTX1133 but noted heterogeneity within the MRTX1133-resistant group, suggesting differential activation of the MAPK pathway across the cohort after tumors acquire resistance to KRAS^{G12D} inhibition (Supplementary Fig. S7C).

Single-nucleus inferred CN profiles were then used to define intratumoral genetic heterogeneity across the KPC cohort ("Methods"). We observed concordance between genomic amplifications found by both WES and snRNA-seq, where the latter revealed the existence of multiple subclones in several tumors [Fig. 4F (right pie charts) and G; Supplementary Fig. S7D]. In a subset of MRTX1133-resistant tumors, putative resistance drivers identified at the bulk DNA level appeared subclonal when analyzed using CN inferred by snRNA-seq (Fig. 4G). In KPC_3323, we observed two distinct clones, with Yap1 amplification identified only in clone 1, representing 48% of the malignant cells within this tumor. In KPC_3600, *Cdk6*/*Abcb1a*/*Abcb1b* was found amplified in a minor clone (clone 3), accounting for 13% of the malignant cells in this sample. In aggregate, we observed putative genetic drivers of resistance in 6/11 tumors analyzed by WES and/or snRNA-seq, including cases of subclonal heterogeneity for these alterations in two tumors (Fig. 4H). As previously suggested from patient data (Fig. 1D), the absence of clear resistance-associated genomic alterations within some subclones or entire tumor samples in our KPC cohort indicates that non-genetic mechanisms may also play an important role in driving acquired resistance to Kras^{G12D} inhibition.

Malignant Cell State Evolution in Response and Resistance to KRAS^{G12D} Inhibition

To identify non-genetic drivers of resistance to Kras^{G12D} inhibition, we next assessed transcriptional variation in malignant cells across tumors in the snRNA-seq dataset (Fig. 5A). Using an established non-negative matrix factorization (NMF) approach (50, 51), we identified 51 high-quality programs across the 17 KPC tumors, grouped into six metaprograms reflecting core cellular processes such as cell cycle and hypoxia, as well as cellular identities along the epithelial–mesenchymal axis, including both classical (epithelial) and mesenchymal cell states (Fig. 5A; Supplementary Fig. S8A–S8C; Supplementary Table S8, "Methods"). We additionally identified a neural-like progenitor signature related to our *de novo* classical metaprogram and resembling a previously described PDAC transcriptional subtype (52). Finally, we identified a novel partial EMT (pEMT) signature analogous to previously described hybrid states along the epithelial–mesenchymal axis (Supplementary Fig. S8A; refs. 50, 53).

Having defined the diversity of malignant metaprograms across KPC tumors (Supplementary Fig. S8A–S8C), we next sought to understand evolution across the core cell states defined by classical, mesenchymal, and pEMT metaprograms by assessing cell state commitment at single nucleus resolution using a Markov absorption-based classification approach ("Methods"; ref. 54). Differential gene expression analysis across cell state populations identified well-defined genes associated with the classical (e.g., *Tff1*, *Tff2*, *Muc5ac*) and mesenchymal states (e.g., *Zeb1*, *Snail1*, *Vim*), as well as hallmark cellular processes and functions upregulated in a cell state–specific manner (Fig. 5B and C). EMT features and high KRAS signaling were observed in the mesenchymal cells, whereas cell cycle processes and increased xenobiotic metabolism were enriched in the classical population. The pEMT cell state was marked by signatures of cellular stress, enhanced translation, protein homeostasis, oxidative phosphorylation, and Myc signaling (Fig. 5C; Supplementary Fig. S8D), several of which have been previously associated with resistance to KRAS pathway suppression or inhibition (5, 55). Finally, we conducted gene regulatory network analysis and identified major transcriptional regulators whose expression and inferred activity associated with metaprogram expression across tumors (Fig. 5D). Along with identifying well-established metaprogram regulators, such as *Zeb1* for mesenchymal or *Spdef* and *Creb3l1* for classical states, we uncovered novel putative regulators of the pEMT cell state, including *Ybx1*, *Sox4*, as well as components of the AP1 complex such as *Jun*, *Junb*, and *Jund*.

Next, we assessed the distribution of nuclei according to treatment and timepoint across the classical-pEMT-mesenchymal tripartite cell state framework (Fig. 5E). Tumors from vehicle-treated KPC mice displayed mixed phenotypic populations along the classical-mesenchymal axis. In the MRTX1133-treated tumors, we observed two distinct patterns of cell state commitment. Tumors in the early (3-day) MRTX1133 treatment cohort demonstrated strong depletion of mesenchymal PDAC cells and enrichment for the classical cell state, suggesting that mesenchymal PDAC cells may be relatively more sensitive than classical PDAC cells to Kras^{G12D} inhibition *in vivo*. This pattern was not observed in any other treatment group. Furthermore, within the MRTX1133-resistant tumors, we observed a profound shift toward the pEMT (60% of nuclei from resistant tumors) and mesenchymal (30% of nuclei from resistant tumors) malignant cell states via snRNA-seq (Fig. 5E; Supplementary Fig. S8E and S8F). Histologic analysis of KPC tumors across treatment groups revealed a strong enrichment of poorly differentiated tumor cells within MRTX1133-resistant tumors (Supplementary Fig. S8G and S8H). We also observed a shift in the distribution of cycling cells along the classical-pEMT-mesenchymal axis in MRTX1133-treated tumors, with classical cells being the predominant cycling population upon early exposure to MRTX1133 treatment and the pEMT and mesenchymal cell states demonstrating a greater fraction of cycling cells at acquired resistance (Supplementary Fig. S8I). Collectively, these data suggest that malignant cell state determines response to KRAS inhibition *in vivo*, with mesenchymal cells displaying greater sensitivity early during treatment and the pEMT metaprogram representing a drug-resistant phenotype that may reflect plasticity from the classical cell state during evolution of resistance to KRAS^{G12D} inhibition.

We further validated the classical state commitment during early MRTX1133 response at the protein level by employing multiplex immunofluorescence (mIF) for the canonical classical state marker Claudin-18.2 (CLDN18.2) across KPC tumors.

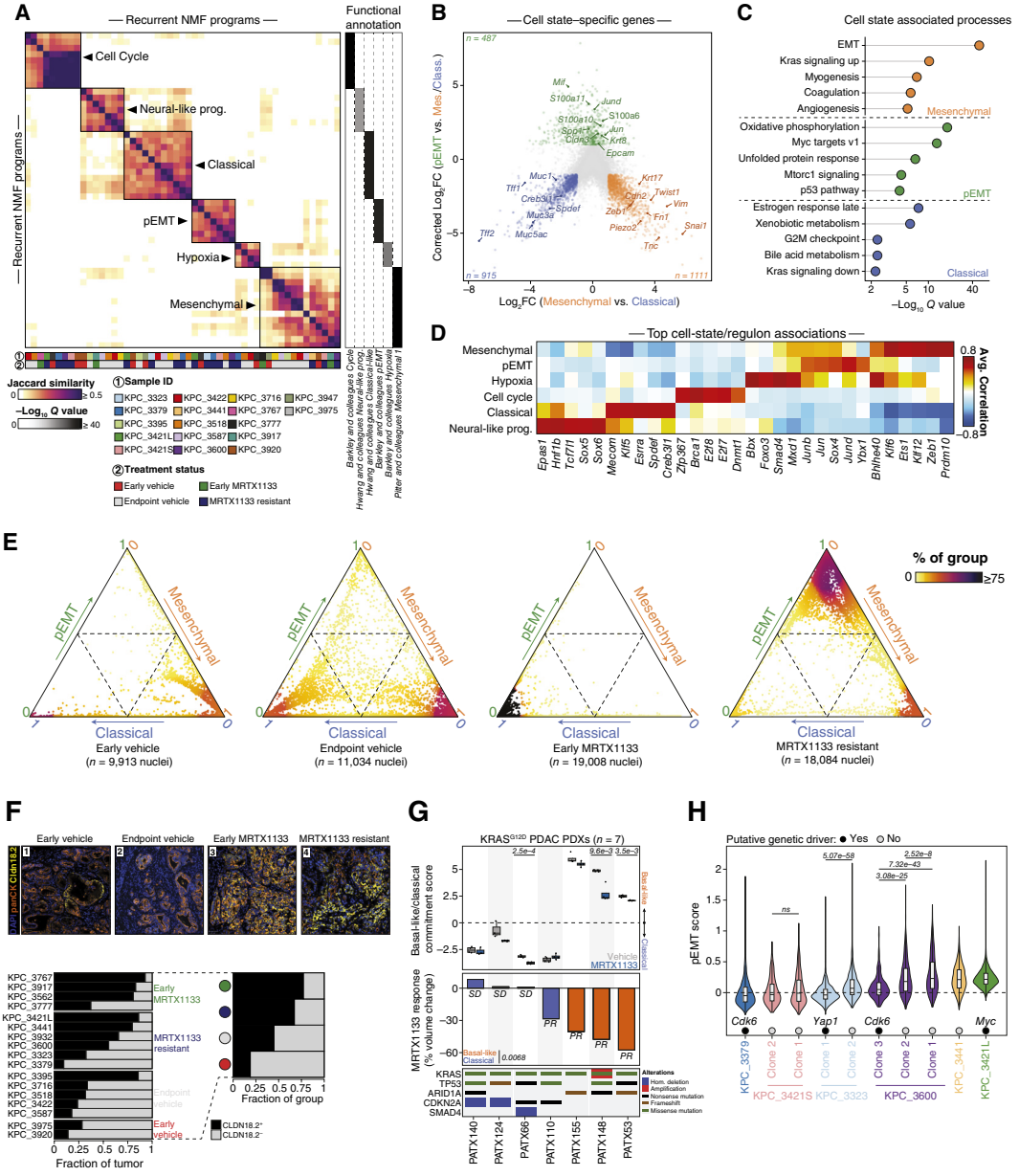

Figure 5. Malignant cell state evolution along the epithelial–mesenchymal axis during response and resistance to MRTX1133 *in vivo*. **A,** Left, Heatmap of pairwise Jaccard similarities between recurrent NMF programs identified across KPC tumors and ordered by hierarchical clustering. Six consensus classifications (metaprograms) are labeled and indicated by squares. Right, Heatmap depicting the top functional annotation for each metaprogram. Significance determined by hypergeometric test and adjusted with Benjamini–Hochberg correction. **B,** Cell state–centered differential gene expression across the mesenchymal, classical, and pEMT malignant cell populations. Cell state–specific upregulated genes are colored, and subsets are labeled. **C,** Top enriched Hallmark gene expression signatures across cell state–specific upregulated genes displayed in **B**. Significance determined by hypergeometric test and adjusted with Benjamini–Hochberg correction. **D,** Heatmap depicting the top five regulons associated with each metaprogram. The average Pearson's correlation coefficients are calculated between each regulon activity scores, as inferred by pySCENIC, and metaprogram scores across malignant nuclei. **E,** Ternary plot displaying the cell state classification probability of each nucleus across the classical-pEMT-mesenchymal tripartite framework, as calculated by a Markov absorption-based classifier ("Methods"). The coloration gradient is proportional to the fraction of nuclei from a given treatment group found in the same neighborhood. **F,** Top, Multiplex immunofluorescence (mIF) of PDAC areas from four representative tumors with overlaid DAPI (nucleus), pan-cytokeratin (panCK, tumor), and Claudin-18.2 immunostaining. The scale bar represents 50 μm. Bottom left, Tumor-wise Claudin-18.2 fluorescence classification across treatment groups via mIF. Bottom right, Treatment-wise classification of Claudin-18.2 expression via mIF. **G,** Improved responses observed in basal-like compared with classical human PDAC PDX models. Top, Boxplot depicting the basal-like/classical difference score for each PDX model following 3-day treatment with the indicated regimen. Significance for the vehicle vs. MRTX1133 comparison was determined by two-sided Student *t* test. The *P* value for the treatment comparison is displayed at the top of each PDX model's track and only significant comparisons are displayed. Middle, Barplot depicting the tumor volume change at endpoint after MRTX1133 treatment, compared to baseline. Significance between basal-like and classical models determined by two-sided Student *t* test. Bottom, Co-mutation plot of recurrently mutated genes in PDAC for each PDX model. **H,** Violin plot depicting the pEMT scores from snRNA-seq across nuclei from MRTX1133-resistant tumors, divided according to subclones as determined by inferred copy number profiles. Genomic amplifications identified by WES and inferCNV are denoted. Scores are compared between subclones within the same tumors. Significance was determined between clones from the same tumor by a two-sided Wilcoxon rank-sum test and adjusted with Benjamini–Hochberg correction. The *P* values are displayed on top of each clone pairs.

Consistent with the classical enrichment at the transcriptional level in the early MRTX1133-treated tumors, we observed enrichment of CLDN18.2 protein expression via mIF in these tumors (Fig. 5F). Interestingly, when compared to vehicle-treated tumors, most MRTX1133-resistant tumors also displayed a relative enrichment of CLDN18.2 (Supplementary Fig. S8J). Thus, response to MRTX1133 is accompanied by classical cell state enrichment, with CLDN18.2 expression upregulated early during response and retained through acquired resistance.

Given the relative sensitivity to KRAS inhibition seen for the mesenchymal population of PDAC in the KPC model, we next sought additional evidence that human PDAC transcriptional subtypes associate with response to MRTX1133 *in vivo*. Human patient-derived xenograft (PDX) models have been shown to faithfully recapitulate human PDAC subtype diversity, including both classical and basal-like subtypes (56), with the basal-like PDAC phenotype showing phenotypic similarities with the mesenchymal cell state in PDAC (57). We therefore examined a collection of $KRAS^{G12D}$-mutant PDX models ($n = 7$) recently reported to demonstrate PR or SD with MRTX1133 treatment (32). We performed transcriptome profiling of these PDX models after 3 days of vehicle or MRTX1133 treatment and determined their baseline basal-like versus classical subtype score using the 3-day vehicle-treated samples. We observed deep regressions and PRs to MRTX1133 in all basal-like models ($n = 3/3$). Conversely, SD was predominantly observed in classical models, with little or no tumor regressions in 3/4 models (Fig. 5G). Additionally, we observed a significant decrease of the basal-like identity upon 3 days of KRAS inhibitor treatment compared to vehicle treatment in 3/7 PDXs (Fig. 5G), thus further supporting observations from our autochthonous KPC cohort (Fig. 5E). These *in vivo* PDX results support a relatively increased response to KRAS inhibition for basal-like PDAC compared to classical PDAC.

Finally, we examined the interplay between putative genetic and non-genetic drivers of resistance to $KRAS^{G12D}$ inhibition. We integrated previously defined genetic subclones (Fig. 4G and H; Supplementary Fig. S7D) and interrogated the distribution of the drug-resistant pEMT metaprogram within individual MRTX1133-resistant tumors (Fig. 5H). In three out of four tumors where a clonal or subclonal putative genomic driver of resistance was detected, we observed relatively lower expression of the pEMT signature. For example, malignant nuclei with *Cdk6/Abcb1a/Abcb1b* amplification displayed relatively low enrichment of the pEMT metaprogram, whether they were derived from a subclone harboring the amplification within a genomically heterogeneous tumor (KPC_3600, clone 3) or from a tumor with a clonal amplification (KPC_3379). Similarly, the *Yap1*-amplified subclone (clone 1) from KPC_3323 also displayed a relatively lower pEMT signature compared with the *Yap1* non-amplified clone 2 of that same tumor. In contrast, other tumors displayed co-occurrence of both a genetic driver and the pEMT phenotype at drug resistance, such as KPC_3421L, displaying a clonal *Myc* amplification and relatively high enrichment of pEMT. KPC_3441 did not harbor any identified genomic driver of resistance, yet exhibited relatively high expression of the pEMT cell state (Fig. 5H). Thus, we observed heterogeneity in the emergence of the pEMT program alongside putative genetic drivers of resistance, with evidence that the pEMT state may serve as a distinct path to resistance in certain tumors or play a complementary role with genetic drivers in other tumors.

Collectively, these data suggest that both genetic and non-genetic mechanisms likely co-evolve during therapy and give rise to tumors with heterogeneous mechanisms of resistance to mutant-selective KRAS inhibition in PDAC.

Efficacy of Combination Chemotherapy with $KRAS^{G12D}$ Inhibition in PDAC

The complex and heterogeneous patterns of resistance mechanisms emerging with single-agent KRAS inhibition suggests that combination therapy with KRAS inhibitors will be necessary to improve the depth and durability of response in advanced disease. We observed a consistent relative greater sensitivity of the mesenchymal/basal-like PDAC cells compared with the classical PDAC cells in both the KPC and PDX models (Fig. 5E and G), thus suggesting that combination strategies targeting vulnerabilities of the classical state may enhance the efficacy of KRAS inhibition. Patient data suggest that the classical subtype of PDAC responds better to chemotherapy than the poorly prognostic basal-like PDAC subtype (44, 58, 59). Thus, we sought to investigate whether combination chemotherapy could significantly improve the efficacy of Kras inhibition in multiple mouse models of primary and metastatic PDAC.

To this end, we orthotopically implanted 6694C2 murine PDAC cells in the pancreas of C57BL6/J mice, and once tumors were detectable by ultrasound, mice were randomized to receive vehicle, gemcitabine/(n)ab-paclitaxel (GnP), MRTX1133, or a combination of both (MRTX1133/GnP). GnP treatment caused modest tumor growth inhibition compared to vehicle-treated animals (Fig. 6A). MRTX1133 monotherapy led to tumor regression, but tumors relapsed after 2 weeks of treatment. Consistent with prior reports (32, 33), short-term treatment with MRTX1133 resulted in increases in $CD4^+$ and $CD8^+$ T cells in this orthotopic model (Supplementary Fig. S9A–S9C). Combination therapy with MRTX1133 and GnP also caused tumor regressions but significantly prevented relapse, with dramatically longer tumor growth inhibition on treatment through the endpoint of the experiment, occurring after more than 50 days of therapy (Fig. 6A). Thus, these data support that combination chemotherapy plus $KRAS^{G12D}$ inhibition leads to significantly improved primary tumor growth control compared to either treatment alone.

Most patients with PDAC present with metastatic disease, and early clinical trials of KRAS inhibitors are largely conducted in this patient subset where chemotherapy is the current standard of care. Thus, we next sought to examine single-agent MRTX1133 and combination treatment with chemotherapy in a novel mouse model of PDAC metastasis. We previously generated a transplantable cell line model of metastatic PDAC (6694C2-LM) by isolating and culturing a tumor nodule from a spontaneous lung metastasis of a 6649C2 tumor-bearing mouse (60). Upon subcutaneous (SC) implantation of 6694C2-LM cells, followed by subsequent resection of the primary tumor and clinical monitoring, mice

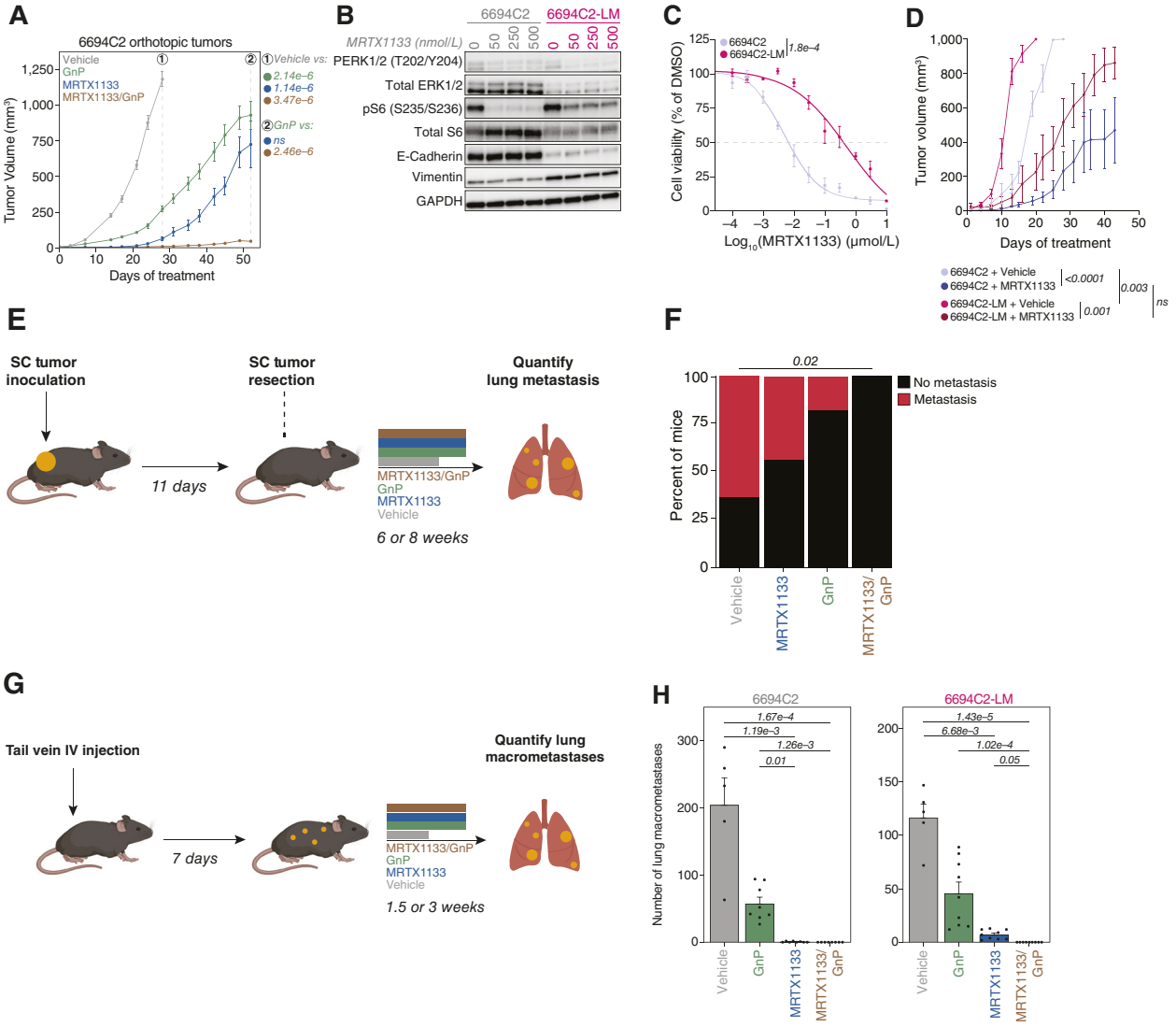

Figure 6. Enhanced efficacy of combination treatment with Kras^{G12D} inhibition and chemotherapy in primary and metastatic PDAC. **A,** Tumor growth kinetics (as measured by ultrasound) of 6694C2 orthotopic pancreatic tumors in C57BL6/J mice treated with the indicated regimens. Comparisons have been done at the endpoint of vehicle treated mice against all other arms (day 28, timepoint 1); and at day 52 for MRTX1133 and MRTX1133/GnP compared to GnP alone (timepoint 2). Significance determined with two-way ANOVA with the Šidák multiple comparisons test. The adjusted *P* values for each timepoint and comparison is displayed on the right. **B,** Immunoblots of the 6694C2 and 6694-LM cell lines treated for 24 hours with the indicated doses of MRTX1133. GAPDH was used as protein loading control. **C,** MRTX1133 dose-response curves for 6694C2 and 6694C2-LM cell lines treated with increasing concentration of MRTX1133 for 5 days. Points are the mean ± SEM of three biological replicates. Significance determined by two-sided Student *t* test between AUCs from three biological replicates from each cell line. **D,** Vehicle and MRTX1133 treatment of animals bearing syngeneic subcutaneous double flank tumors of 6694C2 or 6694C2-LM. Points are the mean ± SEM ($n = 5$ double flanked mice per cell line and treatment). Significance determined by Brown–Forsythe and Welch ANOVA followed by Dunnett's T3 multiple comparisons test. **E,** Overview of the metastatic model. Subcutaneous 6694C2-LM tumors are surgically resected, and mice are monitored for lung metastasis. Adjuvant treatment schedule is shown, with treatment arms including MRTX1133 IP twice daily, gemcitabine treatment every 3 days and (n)ab-paclitaxel on days 13 and 19, or a combination of MRTX1133 and gemcitabine/(n)ab-paclitaxel (GnP). **F,** Percentage of mice within each treatment group presenting with metastasis ($n = 9$–11 mice per group). Significance determined by Fisher's exact test and adjusted with Benjamini–Hocheberg correction. Only significant pairwise comparisons are labeled with a *P* value (*P* value ≤ 0.05). **G,** Experimental workflow to study the effect of GnP, MRTX1133, or combination of both on established metastases from 6694C2 and 6694C2-LM cell lines. **H,** Barplot depicting the total number of lung macrometastases from 6694C2 (left) or 6694C2-LM (right) across treatment groups ($n = 5$–10 mice per cell line and treatment). Significance determined via Kruskal–Wallis test followed by Dunn's test and adjusted with Benjamini–Hochberg correction. Only the significant *P* values are displayed (*P* value ≤ 0.05).

ultimately develop metastatic spread to the lung, lymph nodes, and to a lesser extent the liver (60). *In vitro*, 6694C2-LM is characterized by an increased mesenchymal phenotype compared to its parental line, demonstrated by decreased E-cadherin and increased Vimentin expression at the protein level (Fig. 6B). This line displayed significant resistance to MRTX1133 compared to the parental control (6694C2) *in vitro* (Fig. 6C). *In vivo*, 6649C2-LM implanted subcutaneously grows slightly more rapidly than the parental cell line, showing overall more aggressive growth and faster outgrowth

under MRTX1133 treatment (Fig. 6D). We examined immune infiltrates from mid-stage 6694C2-LM subcutaneous tumors treated with vehicle versus MRTX1133. Consistent with prior work showing that oncogenic KRAS drives production of GM-CSF and recruitment of granulocytes (61, 62), we found that MRTX1133 treatment resulted in reduced immunosuppressive growth factors and reduced infiltration of granulocytic and monocytic myeloid-derived suppressor cells (Supplementary Fig. S10A–S10D). No changes in T cell infiltrates were observed in this poorly immunogenic model.

In the 6694C2-LM metastasis model (Supplementary Fig. S11A), neoadjuvant treatment with either MRTX1133 or GnP led to comparable primary tumor control and prevention of metastasis, whereas adjuvant MRTX1133 treatment alone led to incomplete control of metastatic spread (Supplementary Fig. S11B–S11D). We next evaluated the ability of adjuvant MRTX1133, GnP, or the combination of MRTX1133 and GnP chemotherapy to control metastatic spread. Mice were inoculated with subcutaneous tumors which were then surgically removed at a comparable size across the cohort (Fig. 6E; Supplementary Fig. S11E). Mice were then randomized after surgery and treated with either vehicle for 6 weeks, MRTX1133, GnP, or a combination of MRTX1133/GnP for 8 weeks before sacrifice and organ harvest to examine for metastases. We observed that mice treated with adjuvant vehicle, MRTX1133, or GnP alone developed macrometastatic disease (Fig. 6F). However, the combination treatment of MRTX1133 and GnP reduced metastatic burden to undetectable levels.

Finally, we assessed the efficacy of these treatment regimens on the control of established metastases using an intravenous tail vein injection model of lung metastasis. We injected the metastatic cell line 6694C2-LM or the parental 6694C2. Tumors were allowed to establish in the lungs for 7 days prior to the start of therapy (Fig. 6G). Whereas vehicle-treated mice presented with disseminated lung metastases, GnP treatment reduced the total number of macrometastases (Fig. 6H). Single-agent MRTX1133 significantly reduced the overall metastatic burden compared to GnP alone, with greater efficacy observed in the 6694C2 parental model compared to the more MRTX1133-resistant 6694C2-LM model. In both cases, the combination of MRTX1133 with GnP significantly outperformed all other treatment conditions, with none of the enrolled mice demonstrating lung metastases (Fig. 6H). These results illustrate the benefit of combination chemotherapy with mutant-selective Kras inhibition in an aggressive, metastatic model of PDAC.

DISCUSSION

KRAS inhibitors have the potential to transform the care of patients with PDAC; however, primary and acquired resistance will limit the efficacy and durability of these therapies. Here, we performed a multimodal analysis of clinical samples and preclinical models to define mechanisms of resistance to mutant-selective KRAS inhibition in PDAC. We identified heterogeneous genetic and non-genetic mechanisms of resistance, suggesting multiple combination therapy strategies for future clinical trial design. Moreover, we have generated a suite of novel *in vitro* and *in vivo* models of acquired resistance to $KRAS^{G12D}$ inhibition that may serve as valuable tools for the field to further study resistance mechanisms and evaluate combination therapies.

Leveraging a unique collection of paired pretreatment and post-progression samples from patients with PDAC treated with adagrasib or sotorasib on the KRYSTAL-1 and CodeBreaK100 trials, we performed ctDNA analyses and identified multiple genetic events emerging at acquired resistance, including mutations in *PIK3CA* and *KRAS*, and amplifications in RTKs, *KRAS*, *MYC*, and *CDK6*. A putative mechanism of resistance was identified by ctDNA analyses in approximately half of patients with PDAC, CRC, and NSCLC. Distinct patterns of resistance mechanisms are observed across tumor types, although the mechanistic basis remains poorly defined and requires further study. Notably, several patients did not harbor clear genetic mechanisms of resistance, suggesting a non-genetic etiology of resistance or a sensitivity limitation of ctDNA analyses in these patients.

Across a spectrum of preclinical models, we observed several recurrent mechanisms of resistance to KRAS inhibition. In isogenic *in vitro* models of acquired resistance and in KPC-derived MRTX1133-resistant tumors, we identified concordant copy number gain or amplifications of *Cdk6*/*Abcb1a/b* and *Kras* accompanying resistance, consistent with observations from human ctDNA samples. Moreover, as observed in human ctDNA samples at resistance, no drug-binding mutations in *KRAS* were observed in resistant preclinical models, suggesting that these may not be a major mechanism of resistance in PDAC. Integrative multiomic analysis for biomarkers of resistance in PDAC cell lines and PDO models revealed that EMT and activated PI3K–AKT–mTOR signaling consistently associate with relative resistance to KRAS inhibition. Moreover, evidence of RTK-driven adaptive signaling contributing to baseline and acquired resistance to KRAS inhibition has emerged from our analyses of *in vitro* models and patient specimens, as displayed by recurrent genomic amplifications and functional activation at resistance. Recent work has also highlighted the importance of activation of EGFR and other ERBB family members as an adaptive response and resistance mechanism to KRAS inhibition across cancer types (30, 34, 63). The data presented here support combination therapy utilizing agents targeting this adaptive feedback through one or more RTKs.

The evolution of drug-resistant cell states along the epithelial–mesenchymal axis is a consistent feature across preclinical models; however, we observed potential differences with respect to resistance along this spectrum between *in vitro* and *in vivo* settings. In *in vitro* models, EMT signatures and features associated with a mesenchymal cell state accompany resistance to KRAS inhibition. In the KPC model, we observed enhanced sensitivity and depletion of the frankly mesenchymal cell state in short-term treated tumors. However, we observed re-emergence of the mesenchymal identity, as well as a strong enrichment of a distinct pEMT signature at acquired resistance to $KRAS^{G12D}$ inhibition. These observations suggest that cell state plasticity may play an important role in driving resistance to KRAS inhibition and highlight the potential importance of TME-derived signals in shaping the emergence of drug-resistant malignant cell states *in vivo*.

The pEMT cell state was marked by evidence of activation of MYC and MTORC1 signaling at the transcriptional level, consistent with observations using *in vitro* model systems. Moreover, pEMT cells displayed upregulation of oxidative phosphorylation and multiple stress-related processes, such as protein translation and homeostasis pathways. Notably, some of these features have been previously linked to resistance to KRAS suppression (5). The pEMT metaprogram observed at resistance to KRAS inhibition also resembles similar signatures described in recent cell state atlases of human tumors, suggesting that cells expressing features of this state may be present at baseline, before treatment with a KRAS inhibitor (50, 53). Thus, subclonal heterogeneity of the pEMT state at baseline may promote the emergence of drug resistance, therefore supporting the rational development of combination therapy strategies to target this state. Further work will be needed to fully elucidate the drug-resistant nature of cell states along the EMT spectrum in both preclinical models and human samples.

While both the classical and mesenchymal cell states were recurrently expressed across vehicle-treated tumors, we observed a distinct cell state pattern in MRTX1133-treated tumors. The early 3-day treated tumors, representing tumors responding to $KRAS^{G12D}$ inhibition, displayed a uniquely strong classical polarization, suggesting that the classical identity, enriched for xenobiotic metabolism and cell cycle processes, could provide a fitness advantage upon early exposure to KRAS inhibition *in vivo*. These results are consistent with the enhanced efficacy of MRTX1133 treatment on basal-like versus classical PDAC PDX models presented in this manuscript, as well as our prior observations of basal-classical plasticity in human PDAC organoid models demonstrating that the classical state exhibits less sensitivity to RAS/MAPK pathway inhibition than the EMT-associated, basal-like state (44). At treatment endpoint, the MRTX1133-resistant tumors were strongly committed to the pEMT cell state. The relative absence of classical cells and the pervasive expression of the pEMT phenotype at resistance highlights a potential transition between cell states as one important path to drug resistance. Identifying therapeutic targets to address these drug-resistant cell states remains a top priority.

The observation of classical cell state enrichment in the responding tumors suggests that combination therapy targeting vulnerabilities in this state during response to KRAS inhibition could improve the efficacy and durability of treatment *in vivo*. Identification of the upregulation of CLDN18.2 at the protein level in this KRAS inhibitor-induced classical state as well as in the drug-resistant pEMT cell state yields an important potential therapeutic opportunity. CLDN18.2 is a tight junction protein on the cell surface that is thought to be inaccessible due to its localization between cell membranes of normal epithelial cells; however, in malignant cells, CLDN18.2 expression is increased and dysregulated leading to accessibility for targeting otherwise hidden epitopes. Several CLDN18.2-targeting therapies have demonstrated efficacy in clinical trials for GI cancers, including antibodies, antibody-drug conjugates (ADC), and CAR-T cells (64–66). Thus, these data support the concept of targeting cell surface proteins to treat drug-resistant states and specifically suggest investigating combination therapy with KRAS inhibition and CLDN18.2 targeted therapies in preclinical models and ultimately clinical trials.

We observed striking intertumoral and intratumoral heterogeneity of genetic and non-genetic mechanisms of resistance. Within the KPC model, some tumors harbored amplifications of *Yap1* or *Cdk6/Abcb1a/b* that evolved distinctly from the pEMT drug-tolerant state in either a clonal or subclonal manner. In contrast, we also observed clonal *Myc* amplification emerging concurrently with expression of the pEMT signature at drug resistance. The co-evolution of multiple putative drug-resistance mechanisms within the same tumors mirrors observations in human samples whereby multiple distinct mechanisms have been observed within the same patients (14, 18, 19). This complex landscape of evolving resistance mechanisms presents a challenge when thinking about combination therapies for patients. As noted above, targeting consistently upregulated cell surface proteins with specificity for drug-resistant cell states (e.g., CLDN18.2) represents an attractive strategy for addressing non-genetic mechanisms of resistance. Exploring the therapeutic implications of emerging surface targets associated with the EMT phenotype, including Netrin-1 (67, 68) and CD70 (69), may prove promising in combination with KRAS inhibition. Recent work has also shown that $KRAS^{G12D}$ inhibition leads to an immunogenic response (32, 33); thus, therapies that activate the immune response should be further investigated in combination with KRAS inhibitors in preclinical models and ultimately clinical trials (32, 70).

Furthermore, multiagent chemotherapy is currently the standard of care for the treatment of advanced PDAC, and cytotoxic chemotherapy in combination with KRAS inhibition may address multiple potential resistance mechanisms simultaneously. Additionally, given the relative increased sensitivity to KRAS inhibition of basal-like PDAC and the improved efficacy of chemotherapy on classical PDAC, combination chemotherapy and KRAS inhibition represents an attractive therapeutic strategy. To this end, we demonstrated in multiple PDAC models that the combination of gemcitabine/n(ab)-paclitaxel with $Kras^{G12D}$ inhibition led to improved control of primary and metastatic disease compared with $Kras^{G12D}$ inhibition alone. Therefore, further investigation of combinations involving chemotherapy and KRAS inhibitors is warranted and may present an important strategy for advancing KRAS inhibitor clinical trials to front-line therapy in treatment-naïve patients with PDAC and other KRAS-mutant tumor types.

Limitations of this study include the restriction of the analysis of KRAS inhibitor resistance in human PDAC to primarily ctDNA-based analyses. In the future, it will be critical to obtain biopsies from patients who have progressed on RAS inhibitors, and to fully interrogate these specimens for both genetic and non-genetic mechanisms of resistance. Our preclinical studies have focused on the $KRAS^{G12D}$ inhibitor MRTX1133. Recently developed "pan-RAS" or "pan-KRAS" inhibitors capable of targeting all RAS isoforms or all KRAS alleles will be broadly applicable to most patients with PDAC (71–74). Resistance mechanisms described here are likely to be relevant to many different RAS inhibitors, mutant-selective and otherwise; however, these resistance mechanisms will need to be evaluated with drugs of different selectivity and mechanisms of action to better define patterns of cross-resistance.

Collectively, this study elucidates multiple co-evolving genetic and non-genetic resistance mechanisms that may inform future combination therapy strategies. Additionally, the multimodal approach presented here involving histologic, genomic, transcriptomic, and protein-based analyses of response and resistance in patients and preclinical models may serve as an important paradigm for future translational studies of patients enrolled in clinical trials of novel RAS inhibitors or combination therapies.

METHODS

Patient Data

Defining Acquired Resistance to KRAS^{G12C} Inhibition in Patients. Written and informed consent to institutional review board (IRB)-approved protocols was obtained from patients with KRAS^{G12C}-mutant PDAC and other GI malignancies. All studies were performed in accordance with recognized ethical guidelines, including the Belmont Report and U.S. Common Rule. Patients were enrolled in a phase 1/2 multiple expansion cohort trial of adagrasib in patients with advanced solid tumors with *KRAS*^{G12C} mutation, KRYSTAL-1 (849-001), or in the CodeBreaK 100 phase 1/2 trial to assess the safety and efficacy of sotorasib treatment in patients with KRAS p.G12C-mutated pancreatic cancer who had received at least one previous systemic therapy. Patients who had disease progression while receiving adagrasib or sotorasib monotherapy were included in this study. Patients underwent prescreening for *KRAS*^{G12C} mutation in tumor tissue, performed historically or at the time a patient was considering study entry using sponsor pre-approved methods and laboratories. Platforms used for prescreening tumor mutational analyses included PCR and next-generation sequencing (NGS). Acquired resistance was determined based on routine clinical evaluation by a blinded, board-certified radiologist and defined as SD for at least 12 weeks or a partial or complete response followed by disease progression based on Response Evaluation Criteria in Solid Tumor (RECIST) version 1.1 for CT imaging (75). Institutional review board-approved correlative studies were performed at participating institutions before adagrasib or sotorasib treatment, and at the time of resistance to adagrasib or to sotorasib. IRB-approved correlative studies were performed at participating institutions on ctDNA obtained at the time of resistance, and the results were compared with ctDNA results from pretreatment (Supplementary Table S1).

Patient Sample Collection and Processing. Blood samples were prospectively acquired from patients enrolled to the KRYSTAL-1 (849-001; Patients 1–8, 23–26) or the CodeBreaK 100 (patients 9–22) studies. Peripheral blood (~20–25 mL) was collected in EDTA or Streck BCT tubes, and plasma was obtained by using the Streck IFU. Samples from patients treated with adagrasib on KRYSTAL-1 trial were processed at Resolution Bioscience (now a part of Exact Sciences; patients 1, 2, 3, 5, 6, 7, 23, 24, 25, 26) or at MD Anderson Cancer Center (patients 4, 8). Samples from patients treated with sotorasib on the CodeBreaK-100 trial were processed by Guardant Health (patients 9–22). The genomic panels used for each patient is described below ("ctDNA Sample Processing and Targeted Panel Analysis"; Supplementary Table S1). Blood samples from patients 4 and 8 were processed within a median of 1.5 hours by centrifugation at 2,500 rpm for 10 minutes to separate plasma and buffy coat. A second centrifugation step was performed on the plasma at 5,000 rpm for 10 minutes to remove cell debris. Density gradient centrifugation was used to collect peripheral blood mononuclear cells (PBMC). Buffy coats were processed to extract PBMCs. All centrifugation steps were performed at 4°C. Cell-free DNA (cfDNA) was extracted from 5 mL of plasma samples using QIAamp Circulating Nucleic Acid Kit, according to the manufacturer's protocol. The abundance and quality of cfDNA in the extracted samples were assessed using and bioanalyzer Agilent 2100 Tapestation Cell-free DNA ScreenTape analysis (Agilent) and Qubit 4 Fluorometer (ThermoFisher Scientific). Germline DNA was extracted from 100 µL PBMC with QIAamp DNeasy Blood & Tissue Kit (Qiagen) per manufacturer's instructions.

ctDNA Sample Processing and Targeted Panel Analysis. Pretreatment and EOT ctDNA samples from patients 1, 2, 3, 5, 6, 7, 23, 24, 25, and 26 treated with adagrasib were subjected to the RESOLUTION ctDx FIRST assay developed at Resolution Biosciences (76). Amplifications are identified as an increase in coverage depth. In calling large and moderate amplifications, the estimated tumor copies are required to be 3 (large) or 1 (moderate) more than the tumor ploidy. Longitudinal ctDNA samples from patients 4 and 8, treated with adagrasib, were subjected to a SureSelect Cancer All-In-One custom panel of 58 PDAC-specific genes, designed using SureDesign Tool (Agilent). Pretreatment ctDNA and EOT samples from patients 9 to 22 treated with sotorasib were subjected to Guardant 360 sequencing panel (transferred on May 9, 2022) and were analyzed for emergent variants after treatment with sotorasib 960 mg. Gene alterations considered in the analysis included fusions with *MET*, *EGFR*, *ERBB3*, and *FGFR3* as well as somatic nonsynonymous or splice regions, SNVs or INDELs; and non-aneuploid oncogene copy number gains or tumor suppressor copy number losses. Genomic alterations were represented in relation to the wild-type reference coding sequence and according to the VAF of each specific variant (Supplementary Table S1). From Guardant 360 reports, we called copy number gains when we detected an increase of ≤ 2 copies compared to normal. Amplifications were defined as an increase of >2 copies compared to normal ploidy.

Library Preparation and Analysis of Low-Pass WGS Data. For patients 4 and 8, 10 ng of ctDNA was used as input into SureSelect XT Low Input Target Enrichment System protocol following the manufacturer's instructions. About 10 ng of genomic DNA derived from PBMCs was enzymatically fragmented using the SureSelect Enzymatic Fragmentation Kit (Agilent Technologies). From the same samples, low-pass WGS at an average of 5× depth of coverage was performed to detect CN variants. Libraries were quantified using the Qubit dsDNA High Sensitivity Kit (Invitrogen). The samples were sequenced on a NextSeq 2000 or NextSeq 550 instrument (Illumina). The demultiplexed FASTQ files were analyzed with the SureCall (Agilent) application and the called mutations were uploaded to the Alissa Interpret platform (version 5.3.0, Agilent Technologies) for downstream analysis.

Variant Calling, Tumor Mutational Burden, and CNV Calling from Cell-Free Low-Pass WGS. For patients 4 and 8, we used an ISO27001- and ISO13485-certified platform called Alissa Interpret (Agilent Technologies) and a customized pipeline was created to perform an automated triage to filter and analyze raw genetic variants. For ctDNA samples from patients 4 and 8, tumor mutational burden (TMB) was calculated as the number of mutations divided by the panel size. Synonymous mutations as well as SNVs detected in both ctDNA and PBMC were excluded from the analysis. The sequencing data from low-pass WGS samples were aligned to the human reference genome (version hg38, using bwa mem). Mapped BAM files were processed with HMMcopy's (version 1.44.0) readCounter to create WIG files with 500 kb bins across all chromosomes. WIG files were analyzed with ichorCNA3 to identify CNAs and tumor fractions in cfDNA samples. Segmented data were uploaded to CNApp4 to compute broad, focal, and global CNA scores.

Extracellular Vesicle Isolation from Human Plasma Samples. For patient 4, peripheral blood (~25mL) was collected in EDTA tubes and processed within a median of 1 hour and 30 minutes by centrifugation at 2,500 × rpm for 10 minutes to separate plasma and buffy coat;

followed by an additional 5-minute 5,000 rpm centrifugation at 4°C to remove cellular debris. A total of 4 mL of plasma was processed by ultracentrifugation overnight at 36,000 rpm. The EV pellet was then washed with PBS and centrifuged at 36,000 rpm for 2 to 4 hours. The supernatant was then discarded, and the extracellular vesicle (ev) pellets were resuspended in 600 µL PBS for long term storage at −80°C. Around 200 µL of resuspended EVs were used for RNA extraction using the total exosome RNA & Protein Isolation kit (Invitrogen, cat. #4478545). Contaminating DNA was eliminated using DNase I (Invitrogen, cat. #18047019) while high-abundance human blood globin and ribosomal transcripts were depleted using gRNA/rRNA depletion kit (siTOOLsBiotech, Cat. #dp-K096-001002). All depleted evRNAs were mixed with 1.8 × Ampure RNA Clean XP.

evRNA Transcripts Analysis. A signature matrix generated with expression profiles from normal plasma evRNA and TCGA PDAC tumor samples was utilized to deconvolve the PDAC evRNA, enabling the generation of non-tumor and tumor-derived gene expression profiles by CIBERSORTx (77) and CODEFACS (78). Hallmark KRAS activity signature score was generated at each timepoint using the ssGSEA function implemented in the R package GSVA (version 1.46.0) on DESeq2 (ref. 79; version 1.38.3) log-normalized tumor-derived expression profiles.

Classification of Resistance Mechanisms to KRAS^{G12C} Inhibition Across Cancer Types. We integrated data from patients with PDAC and other GI malignancies from our cohort along with previously published cases of NSCLC, CRC, PDAC, other GI malignancies (including appendiceal adenocarcinoma, ampullary adenocarcinoma, stomach adenocarcinoma, and anal adenocarcinoma), and excluding previously published cases of lung neuroendocrine tumor (patient 105; 14), melanoma, small cell lung cancer and spindle cell carcinoma (patients 10, 21 and 8; 19) to create a pan-cancer cohort of 132 patients with KRAS^{G12C} mutation and displaying acquired resistance to adagrasib, sotorasib, or divarasib (14, 18, 19). Classification of genomic mechanisms of acquired resistance was carried out on a per-patient basis by three independent examiners using treatment-emergent alterations reported in this study (Fig. 1; Supplementary Table S1) or from publicly available data previously mentioned (Supplementary Fig. S1F; Supplementary Table S2).

In Vitro Culture and Experiments

Origins and Genetic Profiling of PDOs. All patients from whom organoids models were derived in this study provided written and informed consent as per IRB-approved protocols at Dana-Farber Cancer Institute (DFCI), permitting access to their clinical and genomic data (DFCI 03189, 14-408). Genetic profiling was performed on the patient's tissue biopsies using WGS or a targeted sequencing panel (OncoPanel), as previously described (44, 80). All organoids utilized in this study were annotated with genomic and clinical information and subsequently utilized in a de-identified, HIPAA-compliant manner.

PRISM Cell Line Screening Assay. The detailed PRISM assay protocol is available online at: https://www.theprismlab.org/. Briefly, the current PRISM cell set consists of more than 900 barcoded cell lines, representing more than 45 lineages, including both adherent and suspension/hematopoietic cell lines. Cell lines were pooled (20–25 cell lines per pool) based on doubling time and frozen in assay-ready vials. MRTX1133 was added to 384-well plates at an 8-point dose range with three-fold dilutions in triplicate starting from 5 µmol/L. Adherent cell pools were plated at 1,250 cells per well, whereas suspension and mixed adherent/suspension pools were plated at 2,000 cells per well. Treated cells were then incubated for 5 days, lysed and mRNAs were isolated. Barcode amplification, detection, and data processing including quality controls were carried out as previously described (43) and yielded high-quality data for a total of 877 cell lines.

Culture and Therapeutic Sensitivity of In Vitro Models

PDAC PDO Models. Organoids were cultured at 37°C in 5% CO_2. Cells were seeded in growth factor reduced Matrigel (Corning; Cat. # 356231) domes and incubated with human complete feeding medium: Advanced DMEM/F12-based-conditioned medium, 1 × B27 supplement, 10 mmol/L HEPES, 2 mmol/L GlutaMAX, 10 mmol/L nicotinamide, 1.25 mmol/L Nacetylcysteine, 50 ng/mL mEGF, 100 ng/mL hFGF10, 0.01 mmol/L hGastrin I, 500 nmol/L A83-01, Noggin 100 ng/mL, 1 × Wnt-3A conditioned 10% FBS DMEM (50% by volume), and 1 × R-spondin Conditioned Basal Medium (10% by volume). For therapeutic sensitivity profiling, organoids were dissociated using TrypLE Express (Thermo Fisher, Cat. #12604054) and cells were seeded into ultra-low attachment 384-well plates (Corning; Cat. #4588) at 1,000 viable cells per well into 20 µL of culture media, consisting of 10% growth factor reduced Matrigel (Corning; Cat. #356231) and 90% human organoid medium as described above. Organoids were treated 24 hours post-seeding over a 12-point dose curve of MRTX1133 (0.1 nmol/L–10 µmol/L) or with DMSO for normalization in a randomized fashion using a Tecan D300e Digital Dispenser (Tecan Trading AG). Cell viability was assessed 6 days post-treatment using a Cell-TiterGlo 3D Cell Viability assay (Promega; Cat. #G9683), executed according to the manufacturer's instructions. Fluorescence was read using a FLUOstar Omega microplate reader. Technical triplicates were conducted for each biological replicate and a total of at least three biological replicates was done for each PDO line.

Cell lines. Human PDAC cell lines were obtained from the Broad Institute Cancer Dependency Map or from American Type Culture Collection (ATCC), and identity was authenticated via STR DNA fingerprinting (Lab corps). The KPCY murine cell lines including 6694C2, 6499C4, 6419C5 were originated from the Stanger lab (81) and cells were split every 2 to 3 days. All cell lines were tested every 3 to 4 months and confirmed to be negative for mycoplasma using Mycostrip Mycoplasma Detection Kit (InvivoGene; Cat. # rep-mys-100) or via PCR (Labcorp). Cells were cultured for at least 1 week post-thaw before experimental use which consisted of one to two passages. Cell lines were cultured at 37°C in 5% CO_2 in Dulbecco's Modified Eagle Medium (DMEM) supplemented with 10% FBS and 1% penicillin/streptomycin (6694C2, 6499C4, 6419C5, PANC-1) or Roswell Park Memorial Institute (RPMI) medium supplemented with 10% heat-inactivated FBS and 1% penicillin/streptomycin (Panc 02.03). For therapeutic sensitivity profiling, cells were seeded either into a 96-well plate (1,000 cells/well, Corning; Cat. # 3903) or a 384-well plate (500 cells/well, Corning; Cat. # 3764). Cell lines were treated post-seeding over a 12-point dose curve of MRTX1133, trametinib, gemcitabine or with DMSO following the same approach described above. Cell viability was assessed 5 days post-treatment using a Cell-TiterGlo 2.0 Cell Viability assay (Promega; Cat. # G9241), executed according to the manufacturer's instructions. Fluorescence was read using a CLARIOstar microplate reader. Technical triplicates were conducted for each biological replicate and a total of at least three biological replicates was done for each cell line. Cell lines subjected to therapeutic combinations were cultured, seeded, treated, and viability was assayed by Cell-TiterGlo 2.0. Bliss synergy scores were calculated using the synergyfinder R package (version 3.6.3; ref. 82).

Generation of Isogenic Models of Acquired Resistance to MRTX1133. MRTX1133-resistant cell lines were generated by continuous dose escalation from as low as 1 nmol/L to 10 µmol/L. Once resistance to MRTX1133 was confirmed, resistant cell lines were routinely maintained in the corresponding medium with 1 µmol/L (10% of the maximum dose reached during the evolution of resistance) of MRTX1133. MRTX1133 was removed 3 to 7 days before starting individual assays.

Immunoblotting. Cells were washed with ice-cold PBS twice, and residual PBS was removed as much as possible. Cells were then lysed with RIPA buffer containing phosphatase and protease inhibitors (ThermoScientific; Cat. # 78440), scraped down the cells, and collected into an Eppendorf tube, mixed well, and kept the tube on ice for 30 minutes. The samples were centrifuged at 13,000 × *g*, 4°C for 20 minutes. The protein concentration was measured by a BCA protein assay kit (Thermo Scientific; Cat. # 23225). An equal amount of protein was loaded to the 4% to 20% Criterion TGX Gel (#5671095) and then transferred to the Immuno-Blot PVDF membrane (Bio-Rad, # 1620177). Protein membranes were incubated with primary antibodies at 4°C overnight and followed by appropriate HRP-conjugated secondary antibody at room temperature for 1 hour. The images were analyzed using ECL substrates (Bio-Rad; Cat. #1705062) under the ChemiDoc Imaging System (Bio-Rad). The antibodies are listed as below: ERK1/2 (cell signaling technology, Cat. # 9102S), pERK1/2 (Thr202/Tyr204; cell signaling technology, Cat. # 9101S), AKT (cell signaling technology, Cat. # 2920S), pAKT (Ser473; cell signaling technology, Cat. # 9271S), S6 (cell signaling technology, #2317S), pS6 (Ser235/236; cell signaling technology, Cat. # 2211S), ZEB1 (cell signaling technology, Cat. # 3396S), Vimentin (cell signaling technology, Cat. # 5741S), E-Cadherin (cell signaling technology, Cat. # 3195S), β-Actin (cell signaling technology, Cat. # 3700S; Supplementary Table S9).

RTK Array. All the procedures were done according to the manufacturer's protocol (R&D systems; Cat. ARY001B). Briefly, isogenic parental and resistant Panc 02.03 were treated with 100 nmol/L MRTX1133 or DMSO. Lysates were collected at 0 hour (DMSO), 5 hours, or 48 hours post-treatment and quantified using a BCA protein assay kit as described above. A total of 200 µg of lysates were incubated with RTK membrane overnight at 4°C, followed by incubation with an Anti-Phospho-Tyrosine HRP Detection Antibody. Finally, individual dot densitometry analysis was conducted using Fiji image analysis software (83).

snRNA-seq Sample Preparation, Library Generation, and Sequencing. Samples were prepared as previously described (52). Briefly, ST stock solution was prepared in nuclease-free water with a final concentration of 146 mmol/L NaCl (Thermo Fisher Scientific, Cat. #M9759), 20 mmol/L Tricine (VWR, Cat #. E170-100G), 1 mmol/L $CaCl_2$ (VWR, Cat. # 97062-820), and 21 mmol/L $MgCl_2$ (Sigma-Aldrich, Cat. #M1028). A total of 2 mL of NST nuclei isolation solution was prepared for each sample by adding 0.2% Nonidet P40 Substitute (Thermo Fisher Scientific, Cat. # AAJ19628AP), 0.01% bovine serum albumin (New England Biolabs, Cat. # B9000S), 0.15 mmol/L of spermine (Sigma-Aldrich, Cat. # S3256-1G), 0.5 mmol/L spermidine (Sigma-Aldrich, Cat. # S2626-1G), and 1:40 Protector RNase Inhibitor (Roche, Cat. # 3335399001) to ST stock. For each specimen, 3 mL working ST buffer was made by adding 1:100 Protector RNase Inhibitor to ST stock. Nuclei resuspension solution (NRS) was prepared by adding 1% BSA (Miltenyi, Cat. # 130 091-376) and 1:40 Protector RNase inhibitor to PBS (Gibco, Cat. # 10010023). Snap-frozen tumor chunks were placed in microcentrifuge tubes with 1 mL NST and manually minced with fine straight tungsten carbide scissors (Fine Science Tools; Cat. # 15514-12) for 8 minutes. Nuclei suspension was then passed over a 30-micron cell strainer (Miltenyi Biotec; Cat. # 130-098-458) into a 15 mL conical tube (ThermoFisher Scientific; Cat. # 339651). Microcentrifuge tubes and strainers were washed with an additional 1 mL NST, then nuclei suspensions were diluted with 3 mL ST buffer. Following this, suspensions were centrifuged for 5 minutes at 500 *g*, 4°C with slow brake. Following inspection of the pellet, the supernatant was removed, and the pellet was resuspended in 150 to 200 µL of NRS and then passed through a FACS tube filter (Falcon; Cat. # 352235). Nuclei were then quantified using a disposable hemocytometer (inCYTO; Cat. # 82030 -472) in brightfield and then diluted or concentrated in NRS, according to the manufacturer's instructions. Single-cell gene expression libraries were generated as previously described (52) and up to 12 samples were pooled per flow-cell and then sequenced on a NovaSeq S2 (Illumina) with the following paired-end read configuration: read 1: 28 nt; read 2: 90 nt; i7 index read: 10 nt; i5 index read: 10 nt.

WES Sample Preparation and Sequencing. For WES of KPC tumors and cell lines, genomic DNA was extracted using Qiagen AllPrep DNA/RNA Mini Kit (Qiagen; Cat. # 80204). WES was performed by MedGenome or Novogene and the library was prepared using Agilent SureSelectXT Mouse All Exon kit and the sequencing was carried out on a NovaSeq (Illumina, PE150).

Bulk RNA-seq Sample Preparation and Sequencing. Parental and MRTX1133-resistant cell lines (Fig. 3) were trypsinized and washed with PBS twice, cell pellets were collected, and total RNA was extracted using the RNeasy Plus Kits for RNA Isolation according to the manufacturer's protocol (Qiagen; Cat. #73404). Total RNA was sent to Novogene for mRNA-seq library preparation and NGS using Illumina NovoSeq. All the conditions and cell lines were prepared in triplicate.

In Vivo Protocols

Mouse Models. All animal treatments and procedures were conducted under approved protocols aligned with guidelines from the Institutional Animal Care & Use Committee (IACUC, protocol 16-015) at Dana-Farber Cancer Institute (DFCI) or MD Anderson Cancer Center. KPC (*Kras*$^{LSL\text{-}G12D/+}$; Trp53$^{LSL\text{-}R172H/+}$; p48-*Cre*) GEMM mice were obtained as a generous gift from Dr. Sunil Hingorani and were bred and maintained in a pathogen-free Animal Resource Facility (ARF) at DFCI. C57BL/6 mice were purchased from Jackson labs (Stock #000664) and nude mice from Charles River. Mice experiments using PDXs were derived as previously described (84).

Tumor Growth Monitoring. KPC mice underwent weekly palpation for tumor detection starting at 8 weeks of age. Upon the palpable detection of tumors, ultrasound imaging (Vevo 3100) was conducted twice a week to track changes in tumor volume. Ultrasound images spanning the full length and width of the detected tumor were acquired in increments of 0.17 to 0.22 mm, depending on tumor size. All images were subsequently imported into the Vevo LAB software (version 5.6.0) for quantification of tumor volume. Every four to five images, the tumor area was manually outlined, allowing the system AI to outline the images in between. Manual adjustments of the outlines performed by the AI were carried out, if necessary. Once the tumors reached a volume between 100 and 300 µL, animals were non-blindly randomized into either the vehicle or MRTX133 treatment groups. For the short-term treatment groups, mice received a total of six doses administered over 3 days and were subsequently sacrificed. Their tumor volume was monitored before the initial and after the last dosing. Endpoint-treated mice were treated until they reached an IACUC-approved humane endpoint presenting clinical signs but not limited to body condition score <2, weight loss >15%, excessive or prolonged hypothermia, dyspnea, dehydration, hypoactivity, hunched posture, ruffled fur. Tumor volumes from KPC, orthotopic PDAC tumors, and PDX models were monitored twice a week by ultrasound imaging.

In Vivo Treatments. MRTX1133 was provided by Mirati Therapeutics Inc. 10% Captisol (Cydex Pharmaceuticals A Ligand Company, RC-0C7-100) in 50 mmol/L QB citrate buffer solution pH 5.0 (Teknova, Q2443) was used to formulate MRTX1133 and vehicle. Formulated MRTX1133 was freshly prepared and stored light-protected at 4°C for up to 1 week. MRTX1133 (30 mg/kg) was administered via intraperitoneal injection, twice per day, at the maximum

in vivo tolerated dose as described by the manufacturer (30, 31), causing no significant cytotoxic side effects during treatment. Gemcitabine/n(ab)-paclitaxel (GnP) treatments are detailed in sections "Metastasis Model" and "Implantation and Treatment of Pancreatic Orthotopic Tumors".

Tumor Harvest and Processing. Mice were sacrificed by CO_2 asphyxiation followed by cervical dislocation. Immediately after death, the tumor was harvested and further processed for downstream experiments including formalin fixation for histopathology and snap freezing for genomic DNA or single nuclei extraction. Formalin-fixed tissues were submitted to Harvard Medical School Rodent Histopathology Core for paraffin embedding. Serial sections of 4 to 5 μm thickness were prepared from the formalin-fixed, paraffin-embedded (FFPE) tissues and used subsequent experiments, including: hematoxylin-eosin (H&E), multiplex immunofluorescence, chromogen-based immunohistochemical staining.

Subcutaneous Tumor Implantation. Resistant cell lines were assessed *in vivo* by performing double flank subcutaneous tumor inoculations of 200,000 cells per tumor with five mice per group per tumor line. Mice were treated with either vehicle or MRTX1133 as previously described, starting once the tumor was palpable (average 4.5 mm^3). Tumors were measured every 3 days and treatment was continued until tumors ulcerated, reached a size of 1,000 mm^3, or mice reached the experimental timepoint, after which mice were sacrificed as previously described.

Patient-Derived Xenografts. PDXs were derived as previously described (84) and tumor fragments ($4 \times 4 \times 4$ mm^3) were implanted on the right hind flanks of female athymic nude mice (Charles River). Treatment started when the tumor volume reached 150 to 250 μL as monitored by caliper measurements. At enrollment, mice were randomized to receive either vehicle (10% Captisol in 50 mmol/L sodium citrate pH = 5) or MRTX1133 (30 mg/kg, MedChemExpress) twice per day IP, as described above. For efficacy studies, treatment groups included six mice per group. For acute pharmacodynamic (PD) biomarker studies ($n = 4$ mice per group), tumors were allowed to grow to an average volume of 250 to 350 mm^3 and collected 4 hours after 3 days of treatment. All animals received LabDiet 5053 chow ad libitum. During the PDX efficacy studies, tumor growth was monitored twice a week, and the tumor volume was calculated as TV = $(D \times d^2/2)$, where "D" is the larger and "d" is the smaller superficial visible diameter of the tumor mass. Body weights were measured twice weekly and used to adjust dosing volume and monitor animal health. All animal studies are reviewed and approved by the Institutional Animal Care and Use Committee (IACUC) at MD Anderson Cancer Center.

Metastasis Model. Metastasis was assessed as published previously (60). In brief, 6694C2-LM cells were subcutaneously injected with 200,000 cells per animal in the shaved lower back. Primary tumors were surgically removed 11 days post-tumor inoculation with collection of lungs, inguinal lymph nodes, and livers to look for metastasis 4 to 8 weeks later. Mice with tumor regrow at the primary site after surgical removal were eliminated from the study. Neoadjuvant treatment was performed starting at day 6 where mice were treated with MRTX1133 twice per day IP, as described above, until the morning of day 11 when surgery was performed or gemcitabine (25 mg/kg, IP) at day 6 and 8 and (n)ab-paclitaxel (30 mg/kg, IV) on day 6. Primary tumors were weighed post-surgery. Adjuvant treatment was started on day 13, 2 days post-surgery, with mice treated twice daily with MRTX1133 for 8 weeks and/or with (n)ab-paclitaxel (30 mg/kg IV) on day 13 and 19 and gemcitabine (25 mg/kg, IP) every 3 days starting on day 13 for 8 weeks or vehicle for 6 weeks. After harvest, macrometastasis was assessed visually by inguinal lymph node size and nodules on the lung while the micrometastatic area was assessed using H&E, processed as above described, scanned on an Olympus VS200 Slide Scanner, and quantified using QuPath (85).

Implantation and Treatment of Pancreatic Orthotopic Tumors. Efficacy of MRTX1133, chemotherapy, and combination of both were assessed in the primary setting by implanting 50,000 6694C2 cells orthotopically into the pancreas of C57BL6/J mice. Once tumors were detectable by ultrasound, 10 mice were randomly assigned to each of four treatment groups wherein they received either vehicle, gemcitabine/n(ab)-paclitaxel (GnP), MRTX1133, or a combination of MRTX1133 and GnP. Mice undergoing GnP treatment were dosed IP every 3 days with gemcitabine (150 mg/kg), along with two intravenous doses of n(ab)-paclitaxel (50 mg/kg), one on the day of enrollment and the other 6 days later. MRTX1133 was administered as previously mentioned. Tumor volume changes were assessed by ultrasound twice per week. Treatment was maintained until tumors reached a maximum diameter of 2 cm in any direction or until mice reached a humane endpoint, at which time they were sacrificed as previously outlined.

Generation and Treatment of Established Metastases. To assess the efficacy of combination chemotherapy and MRTX1133 in the context of established lung metastases, 60,000 6694C2 or 6694C2-LM cells were injected into the tail vein of C57BL6/J mice. After 7 days, five mice per cell line were randomized to the vehicle group and 10 mice were assigned to receive either gemcitabine/n(ab)-paclitaxel (GnP), MRTX1133, or MRTX1133 and GnP. The dosing regimen was the same as described for the orthotopic setting. At defined experimental timepoints, mice were sacrificed and macrometastases were tallied by visually assessing nodules on the lungs.

Tumor Immune Infiltrate Analysis. Tumors were harvested, minced, and incubated in digestion buffer [RPMI (Gibco), 2% FBS, 0.2 mg/mL Collagenase P (Roche), 0.2 mg/mL Dispase (Gibco), and 0.1 mg/mL DNase I (Roche)] for 30 minutes at 37°C. Tumors were dissociated by repetitive pipetting with the collected supernatant placed in a 40-micron cell filter and quenched by cold FACS buffer (PBS with 2% fetal calf serum and 0.5 mmol/L EDTA). The resulting tumor debris and immune cells were centrifuged, washed with PBS, and resuspended in FACS buffer containing a master mix of antibodies. Cells were incubated in the staining mix for 15 minutes at 4°C, washed in PBS, and resuspended in 1% formalin for analysis on a spectral flow cytometer (Sony SP6800). Flow cytometry antibodies were purchased from Biolegend [αCD45 (30-F11), αCD4 (RM4-5), αCD8 (53-6.7), αCD103 (2E7), αLy6C (1A8), αI-A/I-E (M5/114.5.2), αF4/80 (BM8), αSiglecF (E50-2440), αCD11b (M1170), αCD11c (N418), αGR1 (RB6-8C5), αB220 (RA3-6B2)].

Histopathology Assessment. Sections of 4 to 5 μm thickness were prepared as previously mentioned. Brightfield scans of the H&E-stained slides were prepared using the Vectra Polaris Imaging System (PhenoImager HT). To perform quantitative assessment, scans of these slides (.qptiff files) were loaded into QuPath (85), and two separate QuPath projects (.qpproj files) were created; the first project for measuring areas of PDAC, PanIN, ADM, and normal pancreas within the tissue section, and the second project for measuring areas of well, moderate, or poor differentiation within the PDAC areas. For this, the areas of interest were annotated on the .qptiff files with QuPath's brush tool by a research pathologist, and the area measurements (in sq. microns) were exported as a .csv file for further downstream analysis. As a validation step to check any discrepancies, all slides were reviewed independently by an experienced gastrointestinal pathologist to obtain a visual estimation of these area measurements.

Immunohistochemistry. Immunohistochemistry staining was performed using standard staining on 4-µm-thick FFPE tissue sections from KPC mice tumors. Sections were stained for pERK (T202/Y204; Cell Signaling Technology 4376, dilution 1:500) to assess activity levels of the MAPK pathway. Tissue sections were baked at 60°C, deparaffinized, and hydrated with xylene and 100% ethanol, respectively, then underwent heat-mediated antigen retrieval with sodium citrate buffer. Slide staining was performed in a Leica BOND RX Research Stainer (Leica Biosystems). Antigen expression was visualized using DAB-chromogen and slides were counterstained using hematoxylin to visualize the nuclei. Brightfield scans of IHC-stained slides were prepared at 40× resolution using the Vectra Polaris Imaging System (PhenoImager HT). The staining and quality of the tumor tissue was evaluated by a certified pathologist.

Immunohistochemistry Scoring. Scoring was done by visually determining the percentage of marker positivity in invasive tumor areas. The values are the average of several regions selected per sample. The scoring criteria for pERK was as follows: 100% to 76% = 4, 51% to 76% = 3, 26% to 50% = 2, 1% to 25% = 1, 0% = 0. Scores were then normalized to the highest levels of staining observed across all tumors analyzed. Staining accuracy of the scoring was verified by a trained and certified pathologist.

Multiplex Immunofluorescence. A multiplex immunofluorescence (mIF) panel comprising a classical protein marker (CLDN18.2), nuclear marker (DAPI), and epithelial cell marker (pan-cytokeratin) was developed following previously described methodology (86). Secondary Opal polymer HRP anti-rabbit antibodies and Opal fluorophores were used for detecting primary antibodies. Staining was carried out on the Leica Bond RX Research Stainer (Leica Biosystems). The staining protocol comprised sequential cycles of antigen retrieval (Tris/EDTA), protein blocking, primary antibody incubation, secondary antibody incubation, and fluorescent labeling via tyramide signal amplification on whole slides. Overview scans of all mIF slides were prepared at 10× magnification using the Vectra Polaris Imaging System (PhenoImager HT). Slide fluorescent images are then acquired using the PhenoImager HT multispectral imaging system (Akoya Biosciences). After image acquisition and spectral unmixing, each image is visually inspected to ensure that only regions of invasive cancer are selected for analysis and that all regions are free of artifacts and suboptimal staining. Images are then processed using a customized pipeline that employs supervised machine learning to segment tissue into regions of tumor epithelium and surrounding stroma. Within tumor epithelial regions, individual tumor cells are then identified based on joint consideration of morphology and cytokeratin expression. Within the tumor cell compartment, membranous expression of CLDN18.2 is quantified, and cells are classified as positive or negative for each marker using a pathologist-trained machine learning classifier.

Quantification and Statistical Analyses

Compound Response Analysis. For each cell line and patient-derived organoid, we used the R package dr4pl (version 2.0.0) to fit a four-parameter logistic curve to the response across doses of MRTX1133. The AUC was then calculated as the normalized integral as follows:

$$AUC = \frac{\int_{C\,min}^{C\,max} V(c)dc}{C_{max} - C_{min}}$$

This formulation puts AUC values on a scale between 0 and 1, where lower AUC values indicate increased sensitivity to treatment (43).

KPC GEMM Survival Analysis. The survival analysis was conducted using the survival R package (version 3.5-8) and employed a Log-rank test on Kaplan–Meier curves to compare the overall survival between endpoint MRTX1133- and vehicle-treated KPC GEMMs. The MRTX1133-treated mice KPC_3411 and KPC_4076 were censored at day 0 as their endpoint was due to technical reasons but were still included in the analysis (Supplementary Table S7).

MRTX1133 In Vitro Response Groups and Biomarker Discovery. Stratification of *KRAS*^{G12D} mutated cell lines based on responses to MRTX1133 from the PRISM viability screen was generated using a Jenks natural break optimization approach on the AUC values with a number of breaks set to 2. The discovery of biomarkers of response and resistance to MRTX1133 was carried out by integrating previously defined response groups with publicly available datasets from the 23Q4 DepMap release. These included cell line metadata and lineages, Log_2 CN ratios, bulk RNA-seq, and RPPA. For each type of omics, comparisons were done between resistant and sensitive subsets of cell lines using a two-sided Student *t* test. DESeq2 (ref. 79; version 1.28) with adaptive shrinkage (87) was used on raw RNAseq counts to carry out differential gene expression over all detected genes between sensitive and resistant cell lines (Fig. 2) or resistant and parental pairs (Fig. 3). GSEA were performed on the ranked and unfiltered genes based on Log_2FC from differential gene expression analysis between the aforementioned groups, using the fGSEA R package (version 1.24.0; Supplementary Tables S4A and S4B).

Mutation and CNV Identification from Bulk DNA WES. FASTQ files were converted to unmapped Bam (uBAM) files using the GATK paired-fastq-to unmapped-bam Terra workflow (snapshot 10). The Processing-for-variant-discovery-gatk4 Terra workflow (snapshot 10) was used to map the uBAM files to the reference genome (mm10 for mouse-derived tumors and mouse cell lines and hg38 for human cell lines), as well as to mark duplicate reads and to perform base recalibration. Somatic variant calling was performed at a per tumor basis with Terra's mutect2-gatk4 workflow (version 4.1.7.0, snapshot 21). We used the matched parental cell line for *in vitro* models of acquired resistance (6694C2, 6499C4, 6419C5, Panc 02.03, PANC-1; Fig. 3) and a matched sample from normal tissue for KPC derived (Fig. 4). Several samples (KPC_3323, KPC_3421L, KPC_3421S, KPC_3422, KPC_3518, KPC_3587, KPC_3716, KPC_3776) were sequenced at a significantly greater depth than anticipated due to a technical error. To remedy this error, processed BAMs were down-sampled using Picard's DownsampleSam method (snapshot 2 of Terra Workflow GPTAG/ DownsampleBam with a random seed set to 5054) to a desired coverage of 100× to make them comparable with all other WES samples. A custom Terra workflow was used to perform copy number analysis using CNVkit (version 0.9.10) on a per-sample basis using matched normal tissue or parental cell lines as reference for KPC tumors and isogenic models of acquired resistance, respectively.

Bulk RNA-seq Processing and Analysis. FASTQ files for paired parental and resistant cell lines (Fig. 3) were aligned using STAR aligner (version 2.6.1c) with GRCh38 reference for human lines and GRCm38.p6 for mouse lines or to obtain raw read counts. Additional processing to TPMs was performed using RSEM (version 1.3.0) from the rsem_v1-0_BETA_cfg Terra workflow (snapshot 6). Differential gene expression analysis on the raw counts was performed as previously described (*section:* MRTX1133 *in vitro* response groups and biomarker discovery). Bulk transcriptomic profiles of PDX models were obtained by Quant-Seq. Briefly, RNA was extracted from SNAP frozen tissues, and RNA sample quality was assessed by RNA ScreenTape on a 4200 Tapestation (Agilent Technologies Inc.,) and quantified by Qubit 2.0 RNA HS assay (ThermoFisher). The library was constructed using QuantSeq 3′ mRNA-Seq Library Prep Kit FWD for Illumina (Lexogen). Final libraries quantity was assessed by Qubit 2.0 (ThermoFisher) and quality was assessed by TapeStation HSD1000 ScreenTape (Agilent Technologies Inc.). The average final library

size was about 320 bp with an insert size of about 200 bp. Illumina 6-nt single indices were used. Equimolar pooling of libraries was performed based on QC values and sequenced on an Illumina HiSeq (Illumina) with a read length configuration of 150 PE. Read 1 reads were trimmed using Trimmomatic v0.39 and BBDuk from BBTools v.38.34. Human and mouse reads were identified using Xenome v.1.0.1 with genome references hg38 and mm10, respectively. Human reads were mapped and counted using Kallisto (version 0.44.0) and the genecode.v31 transcript index. Counts were then transformed to counts per million and $\log_2$-transformed with a pseudocount of 1.

snRNA-seq Data Preprocessing. BCL files were converted to FASTQ using Illumina's BCL Convert Tool. CellRanger (version 7.0.1) was used to demultiplex the FASTQ reads and align them to the mm10 mouse transcriptome (mm10_premrna-1.2.0). We then used CellBender remove background (version 0.2.0) Terra workflow (snapshot 11) to remove ambient RNA and other technical artifacts from the count matrices. We used a false positive rate of 0.01 along with a number of epochs ranging between 150 and 200 and a learning rate comprised between 5e–5 and 1e–4. We set the parameters "expected cells" based on the estimated number of cells from the CellRanger output. For downstream analyses, we used CellBender's filtered output file (out_filtered.h5). Next, we filtered the combined gene expression matrix to only include high-quality nuclei using the following criteria: total genes in [400–6,000], total counts in [1,000–35,000], percent mitochondrial counts <5%, percent ribosomal counts <5%, cellular complexity ($\log_{10}$ genes per UMI) >0.8. We identified doublets at a per-sample basis using the quality control filtering steps previously mentioned in combination with DoubletFinder (version 2.0.3) and removed them from each gene×nuclei expression matrices. We additionally removed genes that were not detected in at least 100 nuclei across the entire dataset. Next, UMI counts were then normalized by the total number of UMIs per nucleus and multiplied by a scaling factor of 10,000. Normalized counts were then log transformed for downstream analyses using the R package Seurat (version 5.0.0). Log normalized counts were then scaled while regressing out the total number of counts and genes per nuclei and were used to perform PCA over the top 3,000 most variable genes. We subsequently used the first 50 principal components (PC) to build a k-nearest neighbor (knn) graph (k = 20) and identify clusters by using the Leiden algorithm (resolution = 0.9) and visualized individual nuclei using uniform manifold approximation and projection (UMAP) projection (n.neighbors = 20). These steps were iteratively repeated to identify and filter out remaining poor-quality nuclei from the dataset. Subsequently, we annotated distinct cellular populations identified in the previous steps using known cell-type specific gene markers and defined putative malignant epithelial nuclei based on the expression of epithelial markers, in combination with membership in sample-specific clustering, to be used as observation sets in inferCNV. A similar workflow was implemented for the exploration and analysis of the malignant and TME compartments, separately. After isolating the population of interest, we re-scaled the data and ran PCA. For malignant nuclei, we used the first 50 PCs to build a knn graph (k = 20) and clustered using the Leiden algorithm (resolution = 0.6) followed by dimensionality reduction via UMAP (n.neighbors = 20). For the TME cohort, single nuclei profiles were integrated across samples via Harmony (version 1.2.0), and the first 20 harmonized PCs were retained to build a knn graph (k = 20) and carry out clustering using the Leiden algorithm (resolution = 0.5), followed by dimensionality reduction via UMAP (n.neighbors = 20). CAF- and TAM-specific analyses were carried out following the same approach (Supplementary Fig. S6).

Single-Nucleus CNA Inference and Malignant Classification. The InferCNV Terra workflow (snapshot 15) was used to infer large-scale CNAs from snRNA-seq. The workflow was run on a per-sample basis using CellBender-corrected counts and using a reference population of 1,500 high-confidence non-malignant nuclei evenly and randomly sampled from TAMs, ECs, and CAFs across the cohort. InferCNV was run under the following parameters: cutoff = 0.1, window_length = 101, analysis_mode = subclusters, denoise = TRUE, HMM = TRUE, tumor_subcluster_pval = 0.01. Subclonal clustering was carried out using the Leiden clustering and high probability alterations were identified by using a six-state Hidden Markov Model (i6-HMM) with a stringent probability cutoff (BayesMaxPNormal = 0.2). Nuclei were classified as malignant at a per-sample basis, using the top 10% altered putative malignant nuclei as reference, following the approach previously described, in combination with membership of nuclei to sample-specific SNN clusters (Supplementary Fig. S6D and S6E). Putative drivers of resistance previously identified as amplified via WES were defined as subclonal if present in an i6-HMM state 6 in a single clone, as identified via inferCNV subcluster analysis, within a tumor (*Yap1*: KPC_3323 clone 1. *Cdk6/Abcb1a/*Abcb1*b* in KPC_3600 clone 3).

Calculating and Comparing Signature Scores. Signature scores were computed as previously described (44), by taking a set of genes defining a signature and comparing their average relative expression to that of a control set (n = 100 genes) randomly sampled to mirror the expression distribution of the genes used for the input, as implemented in Seurat's AddModuleScore function. Single-nucleus signature scores were compared across groups by implementing a linear mixed-effect model using the R package lme4 (version 1.1-35.1). The sample ID was used as a random effect and the treatment group or malignant cell state classification, as well as the mouse sex, were used as fixed effect covariates. Pairwise group comparisons were conducted using the estimated marginal means derived from the linear mixed-effect model with the R package emmeans (version 1.10.0; Supplementary Fig. S7B).

Identification of Recurrent Gene Expression Programs. Transcriptional diversity within malignant nuclei was studied using NMF as previously described (50, 51). Each sample was processed separately and the corresponding gene × nuclei expression matrix was filtered to retain protein-coding genes (excluding genes encoding for mitochondrial and ribosomal transcripts) captured in at least 1% of the nuclei within that specific sample. NMF was run over a range of k parameters [k in (4–9)] using the sklearn.decomposition (version 1.3.1) implementation in Python 3.10.8. For each sample, the algorithm was run 100 times and the factorization yielding the lowest reconstruction error based on Frobenius beta loss method was kept. This generated a total of 39 NMF factors per sample, later referred to as programs, then summarized by their top 50 weighted genes. We then defined a program as "robust" following previously established criteria (50, 51):

1 Has at least 80% overlap at the gene level with a program obtained within the same tumor using a different factorization value.
2 Has at least 40% overlap with a program analyzed from another tumor.
3 A "founder" program was defined for each set of overlapping programs (step 1) by selecting that with the highest overlap with a program identified in another tumor.
4 Is nonredundant within the same tumor: Once the robust program was defined using the above criterion, any other program within the same tumor with >20% and <80% overlap with the selected robust program was removed.

This resulted in the obtention of 54 robust programs which were then clustered using (1-pairwise Jaccard similarity) as distance metric and the average linkage method. Manual inspection of the hierarchical clustering results allowed the definition of seven clusters, referred to as metaprograms. We defined the gene lists for each metaprogram by selecting the top 50 genes based on the number of occurrences and average weight across robust programs within the same

metaprogram. We then used signatures from MsigDB including Hallmark (H), Reactome (C2:REACTOME), Biocarta (C2:BIOCARTA), Kyoto Encyclopedia of Genes and Genomes (KEGG; C2:KEGG). We additionally used a panel of PDAC transcriptional subtype signatures as well as multiple curated gene sets from the previously published work (44, 50, 52, 53, 88–91). The degree of overlap between gene signatures or metaprograms with other publicly available signatures was assessed using a hypergeometric test and defined as significant with a Qvalue threshold of 0.05 (Benjamini–Hochberg). We then annotated each metaprogram based on recurrent biological themes among the significantly associated signatures. In the process, removed MP2 from further analysis as it contained genes associated with immune effector functions and processes (*Ptprc*, *Ebf1*, *Tbxas1*, *Lyn*, *Mertk*, *Inpp5d*, *Apobec1*, *Rftn1*, *Cd84*, *Ly86*, *Mrc1*, *Lcp1*, *Fyb*; Supplementary Table S8).

Gene Regulatory Network Analysis to Nominate Putative Metaprogram Regulators. Transcription factor activity was characterized on a per-sample basis using pySCENIC (version 0.12.1) and following the standard workflow. After an initial gene filtering of the expression matrix to retain genes captured in at least 1% of the nuclei from a sample. Correlation networks between mouse transcriptional factors and potential targets were calculated with GRNBoost2 from Arboreto (version 0.1.6) and sets of genes co-expressed with TFs were identified based on the correlation networks and compiled into regulons. Next, cis-regulatory motif analysis was performed using RcisTarget with mm10 cisTarget databases v10 containing two gene-motif rankings: 10 kb around the TSS (transcription start site) and 500 bp upstream and 100 bp downstream of the TSS. Regulon activity was then scored in each cell using the AUCell (version 1.6) package. Next, we calculated the average Pearson correlation between regulons activity and metaprogram scores within samples contributing to that metaprogram (Fig. 5A). Then, on a per metaprogram basis, we selected the top five regulons which activity was the most highly correlated with the metaprogram score and these transcription factors were defined as putative regulators of that metaprograms (Fig. 5D).

Malignant Cell State Classification. Single nuclei were classified across the mesenchymal, classical, and pEMT cell states in two steps. First, we classified nuclei into one of the three cell states using nearest template prediction as implemented in the R package CMScaller (version 2.0.1) and the list of genes of each of the cell states. Next, we selected nuclei that were confidently classified into a given cell state (Qvalue, BH < 0.01) and randomly sampled 2,000 nuclei within each group, which were subsequently used to train a Markov absorption-based classifier over the first 50 PCs using the "Classify" function from Phenograph (version 1.5.2; $k = 20$). Output probabilities were subsequently used for visualization (Fig. 5E).

Malignant Cell State Differential Gene Expression Analysis. We implemented a negative binomial gamma mixed effect model using the R package Nebula (version 1.5.1) to identify genes differentially expressed between each malignant cell state, based on Phenograph classifications. The sample ID was used as random effect, the treatment status and the mouse sex were used as fixed effect covariates, and the log-normalized total counts were used as an offset (Fig. 5B). Next, to enrich for genes whose expression is specific to the pEMT cell state and exclusive to mesenchymal and classical cell states, we corrected the Log_2FC values of the pEMT versus others (Mesenchymal + Classical) comparison by the absolute Log_2FC value of that from the mesenchymal and classical comparison. Genes were defined as differentially expressed and specific to a cell state with the following thresholds: Qvalue (BH) < 0.01, abs(Log_2FC) > 1 (for classical and mesenchymal cell states), or corrected $Log_2FC > 1$ (for pEMT cell state). Enrichment of biological processes in each cell state was carried out using a hypergeometric test with the MsigDB mouse Hallmark gene set database.

Data Availability

The data generated in this study are available within the article and its supplementary data files. Raw and processed snRNA-seq and bulk RNA-seq data reported in this article have been deposited at the NCBI Gene Expression Omnibus with accession numbers GSE269313 and GSE269985. All other raw data are available upon request from the corresponding author.

Authors' Disclosures

H. Lyu reports grants from Break Through Cancer during the conduct of the study; grants, personal fees, and non-financial support from Boehringer Ingelheim outside the submitted work. M.P. Kim reports personal fees from PanTher Therapeutics and Olympus, Inc. outside the submitted work. B.Z. Stanger reports non-financial support from Mirati Therapeutics during the conduct of the study; grants from Revolution Medicine and Boehringer Ingelheim outside the submitted work. S. Cristea reports grants from Dana-Farber Cancer Institute and non-financial support from Dana-Farber Cancer Institute during the conduct of the study. S.W. Lowe reports personal fees and other support from ORIC Pharmaceuticals, Blueprint Medicines, and PMV Pharmaceuticals, personal fees from Fate Therapeutics, personal fees and other support from Mirimus, Inc., other support from Senescea and Faeth Therapeutics outside the submitted work. E.M. Van Allen reports personal fees from Tango Therapeutics, Genome Medical, Genomic Life, Monte Rosa Therapeutics, Manifold Bio, and Enara Bio, grants and personal fees from Novartis Institute for Biomedical Research, grants from BMS, personal fees from Serinus Bio, grants from Janssen, personal fees from Foaley & Hoag, personal fees from Riva Therapeutics, grants from Sanofi, personal fees from TracerDx, and grants from NextPoint outside the submitted work; in addition, E.M. Van Allen has a patent for Institutional patents filed on chromatin mutations and immunotherapy response, and methods for clinical interpretation pending. J.D. Mancias reports grants from Novartis, personal fees from Third Rock Ventures and Skyhawk Therapeutics, and non-financial support from Casma Therapeutics outside the submitted work. E. Chan reports other support from Amgen during the conduct of the study; other support from Amgen outside the submitted work. A. Anderson reports other support from Amgen during the conduct of the study. Y.V. Katlinskaya reports employed by Amgen. A.K. Shalek reports compensation for consulting and/or scientific advisory board membership from Honeycomb Biotechnologies, Cellarity, Ochre Bio, Relation Therapeutics, Fog Pharma, Passkey Therapeutics, FL86, Bio-Rad Laboratories, IntrECate Biotherapeutics, Third Rock Ventures, Pfizer, Santa Ana, Sail Biosciences and Dahlia Biosciences unrelated to this work. Dr. Shalek also reports research support from Break Through Cancer, Wellcome Leap, NIH, the Bill & Melinda Gates Foundation, Foundation MIT, the Moore Foundation, the Chan Zuckerberg Initiative, and Becton, Dickinson, and Company also unrelated to this work. D.S. Hong reports other support from Revolution Medicine, grants and other support from Mirati Therapeutics, other support from Amgen, Quanta, and 280Bio during the conduct of the study; and Research(Inst)/Grant Funding (Inst): AbbVie, Adaptimmune, Adlai-Nortye, Amgen, Astelles, AstraZeneca, Bayer, Biomea, Bristol-Myers Squibb, Daiichi-Sankyo, Deciphera, Eisai, Eli Lilly, Endeavor, Erasca, F. Hoffmann-LaRoche, Fate Therapeutics, Genentech, Genmab, Immunogenesis, Infinity, Kyowa Kirin, Merck, Mirati, Navier, NCI-CTEP, Novartis, Numab, Pfizer, Pyramid Bio, Revolution Medicine, SeaGen, STCube, Takeda, TCR2, Turning Point Therapeutics, VM Oncology; Travel, Accommodations, Expenses: AACR, ASCO, CLCC, Bayer, Genmab, SITC, Telperian; Consulting, Speaker, or Advisory Role: 28Bio, Abbvie, Acuta, Adaptimmune, Alkermes, Alpha Insights, Amgen, Affini-T, Astellas, Aumbiosciences, Axiom, Baxter, Bayer, Boxer Capital, BridgeBio, CARSgen, CLCC, COG, COR2ed, Cowen, Ecor1, EDDC, Erasca, Exelixis, Fate Therapeutics, F. Hoffmann-La Roche, Genentech, Gennao

Bio, Gilead, GLG, Group H, Guidepoint, HCW Precision Oncology, Immunogenesis, Incyte Inc., Inhibrix Inc., InduPro, Janssen, Jounce Therapeutics Inc,Lan-Bio, Liberium, MedaCorp, Medscape, Novartis, Numab, Oncologia Brasil, ORI Capital, Pfizer, Pharma Intelligence, POET Congress, Prime Oncology, Projects in Knowledge, Quanta, RAIN, Ridgeline, Revolution Medicine SeaGen, Stanford, STCube, Takeda, Tavistock, Trieza Therapeutics, T-Knife, Turning Point Therapeutics, WebMD, YingLing Pharma, Ziopharm Other ownership interests: CrossBridge Bio (Advisor), Molecular Match (Advisor), OncoResponse (Founder, Advisor), Telperian (Founder, Advisor). S. Pant reports Consulting or advisory role Ipsen Novartis Janssen Boehringer Ingelheim AskGene Pharma BPGbio Jazz Pharmaceuticals AstraZeneca US WorldMeds Nihon Medi-Physics Co., Ltd. Alligator Bioscience Revolution Medicines Arcus Biosciences. P. Olson reports other support from Mirati Therapeutics during the conduct of the study. T.P. Heffernan reports other support from Break Through Cancer during the conduct of the study; other support from Boehringer Ingelheim, Taiho Pharmaceuticals, Blueprint Medicines, and Nexo Therapeutics, personal fees from Psivant Therapeutics, Isomorphic Labs, and Cullgen Inc., outside the submitted work. J.G. Christensen reports personal fees from Mirati Therapeutics and Bristol Myers Squibb during the conduct of the study; personal fees from Mirati Therapeutics and Bristol Myers Squibb outside the submitted work; in addition, J.G. Christensen has a patent 10,633,381 pending and issued, a patent 20220331324 issued, and a patent 10,125,134 issued. A. Maitra reports grants from Break Through Cancer and Sheikh Khalifa bin Zayed Foundation during the conduct of the study; other support from ThriveEarlier Detection, an Exact Sciences Company, and Tezcat Biosciences outside the submitted work. B.M. Wolpin reports personal fees from Ipsen and Mirati, grants and personal fees from Revolution Medicines, grants from Novartis, personal fees from GRAIL, grants and personal fees from Harbinger Health, personal fees from Third Rock Ventures, EcoR1 Capital, grants from AstraZeneca and Eli Lilly outside the submitted work. S. Raghavan reports grants from Microsoft outside the submitted work; and equity in Amgen. P.S. Winter reports other support from Microsoft outside the submitted work. S.K. Dougan reports grants from Novartis, BMS, and Takeda, personal fees and other support from Kojin Therapeutics, and other support from Axxis Bio outside the submitted work. A.J. Aguirre reports grants and personal fees from Mirati Therapeutics and non-financial support from Amgen during the conduct of the study; personal fees from Affini-T Therapeutics, Anji Pharmaceuticals, and AstraZeneca, grants and personal fees from Boehringer Ingelheim, personal fees from Kestrel Therapeutics and Merck & Co., Inc., grants and personal fees from Nimbus Therapeutics, personal fees from Plexium, Quanta Therapeutics, and Reactive Biosciences, grants and personal fees from Revolution Medicines, personal fees from Riva Therapeutics and Servier Pharmaceuticals, grants and personal fees from Syros Pharmaceuticals, personal fees from T-knife Therapeutics, Third Rock Ventures, and Ventus Therapeutics, grants from Bristo Myers Squibb, Deerfield Inc., Eli Lilly, Novartis, and Novo Ventures outside the submitted work. No disclosures were reported by the other authors.

Authors' Contributions

J. Dilly: Conceptualization, formal analysis, data curation, software, investigation, visualization, writing–original draft, writing–review and editing, supervision, methodology, project administration. **M.T. Hoffman:** Conceptualization, formal analysis, data curation, software, validation, investigation,visualization, writing–original draft, writing–review and editing, supervision. **L. Abbassi:** Investigation, writing–review and editing, project administration. **Z. Li:** Conceptualization, validation, investigation, writing–review and editing, supervision. **F. Paradiso:** Investigation, visualization, writing–review and editing, methodology, project administration. **B.D. Parent:** Formal analysis, data curation, validation, investigation, writing–review and editing. **C.J. Hennessey:** Validation, investigation, writing–review and editing. **A.C. Jordan:** Investigation, writing–review and editing. **M. Morgado:** Formal analysis, data curation, software, validation, writing–review and editing, methodology. **S. Dasgupta:** Conceptualization, formal analysis, data curation, software, validation, writing–review and editing, methodology. **G.A. Uribe:** Formal analysis, data curation, validation, investigation, writing–review and editing. **A. Yang:** Conceptualization, investigation, writing–review and editing, supervision, methodology. **K.S. Kapner:** Formal analysis, data curation, software, investigation, visualization, writing–review and editing, methodology. **F.P. Hambitzer:** Validation, investigation, writing–review and editing. **L. Qiang:** Investigation, writing–review and editing. **H. Feng:** Validation, investigation, writing–review and editing. **J. Geisberg:** Formal analysis, data curation, software, methodology, **J. Wang:** Investigation, writing–review and editing. **K.E. Evans:** Validation, investigation, writing–review and editing. **H. Lyu:** Conceptualization, data curation, investigation, writing–review and editing, supervision, methodology, resources, project administration. **A. Schalck:** Formal analysis, data curation, software, investigation, visualization, writing–review and editing. **N. Feng:** Investigation, writing–review and editing. **A.M. Lopez:** Investigation, writing–review and editing. **C.A. Bristow:** Formal analysis, data curation, investigation, writing–review and editing. **M.P. Kim:** Data curation, investigation, writing–review and editing. **K.I. Rajapakshe:** Formal analysis, data curation, software, writing–review and editing, methodology. **V. Bahrambeigi:** Formal analysis, data curation, software, writing–review and editing. **J.A. Roth:** Writing–review and editing, project administration. **K. Garg:** Formal analysis, data curation, software, writing–review and editing, methodology. **P.A. Guerrero:** Formal analysis, data curation, writing–review and editing, project administration. **B.Z. Stanger:** Writing–review and editing, resources. **S. Cristea:** Writing–review and editing, supervision. **T. Baslan:** Investigation, writing–review and editing. **E.M. Van Allen:** Writing–review and editing, supervision. **E. Chan:** Writing–review and editing, resources, project administration. **A. Anderson:** Formal analysis, data curation, software, writing–review and editing, methodology, resources, project administration. **A.K. Shalek:** Formal analysis, data curation, writing–review and editing. **D.S. Hong:** writing–review and editing. **S. Pant:** Writing–review and editing, resources, project administration. **J. Hallin:** Formal analysis, data curation, investigation, writing–review and editing, resources. **K. Anderes:** Formal analysis, data curation, investigation, writing–review and editing, resources, project administration. **P. Olsen:** Investigation, writing–review and editing, supervision, resources, project administration. **T.P. Heffernan:** Conceptualization, investigation, writing–review and editing, supervision, resources, project administration, funding acquisition. **S. Chugh:** Writing–review and editing, supervision. **J.G. Christensen:** Formal analysis, data curation, investigation, writing–review and editing, supervision, methodology, resources, project administration. **A. Maitra:** Formal analysis, data curation, investigation, writing–review and editing, supervision, methodology, resources, project administration, funding acquisition. **B.M. Wolpin:** Formal analysis, data curation, investigation, writing–review and editing, supervision, methodology, resources, project administration, funding acquisition. **S. Raghavan:** Conceptualization, formal analysis, data curation, visualization, writing–original draft, writing–review and editing, supervision. **J.A. Nowak:** Conceptualization, formal analysis, data curation, investigation, visualization, writing–review and editing, supervision, methodology, resources, project administration, funding acquisition. **P.S. Winter:** Conceptualization, visualization, writing–original draft, writing–review and editing, supervision. **S.K. Dougan:** Conceptualization, formal analysis, data curation, investigation, visualization, writing–original draft, writing–review and editing, supervision, resources, project administration, funding acquisition. **A.J. Aguirre:** Conceptualization, formal analysis, data curation,

investigation, visualization, writing–original draft, writing–review and editing, supervision, resources, project administration, funding acquisition.

Acknowledgments

The authors acknowledge Dr. Sunil Hingorani for his gift of the C57/Bl6 KPC mice and the Microscopy Resources on the North Quad (MicRoN) core at Harvard Medical School for microscope use in image analysis. The authors thank Kazuki Takahashi and Jaclyn Varga-Wiles for critical review of the manuscript and assistance with manuscript revisions. J. Dilly is funded by the Pancreatic Cancer Action Network. A. Maitra, P.A. Guerrero, and F. Paradiso are funded by the Sheikh Khalifa bin Zayed Foundation, Break Through Cancer, P50CA221707, R01CA218230. L. Qiang was funded by a SITC-Bristol Myers Squibb Postdoctoral Cancer Immunotherapy Translational Fellowship and by the Claudia Adams Barr Foundation. S.R. was funded by NCI K08 CA260442, the Claudia Adams Barr Program in Innovative Basic Cancer Research, and the Hale Family Center for Pancreatic Cancer Research. A.J. Aguirre., B.M. Wolphin., J.A. Nowak, S.K. Dougan, and J.D. Mancias were funded by the Hale Center for Pancreatic Cancer Research and by Break Through Cancer Foundation. S.K. Dougan and A.J. Aguirre were also funded by U01 CA274276. S.K. Dougan was funded by R01AI158488 and R01AI169188 and by the Ludwig Center at Harvard. A.J. Aguirre is also funded by Break Through Cancer, the Lustgarten Foundation, the Pancreatic Cancer Action Network, NIH-NCI P50CA127003, U01 CA274276, R01 CA276268, and the Dana-Farber Cancer Institute Hale Center for Pancreatic Cancer Research. This work was funded in part with support from Mirati Therapeutics Inc. Schematic and illustrations were created using BioRender.

Note

Supplementary data for this article are available at Cancer Discovery Online (http://cancerdiscovery.aacrjournals.org/).

Received February 4, 2024; revised May 8, 2024; accepted June 27, 2024; published first July 5, 2024.

REFERENCES

1. Siegel RL, Miller KD, Jemal A. Cancer statistics, 2017. CA Cancer J Clin 2017;67:7–30.
2. Hidalgo M. Pancreatic cancer. N Engl J Med 2010;362:1605–17.
3. Papke B, Der CJ. Drugging RAS: know the enemy. Science 2017;355:1158–63.
4. Moore AR, Rosenberg SC, McCormick F, Malek S. RAS-targeted therapies: is the undruggable drugged? Nat Rev Drug Discov 2020;19:533–52.
5. Viale A, Pettazzoni P, Lyssiotis CA, Ying H, Sánchez N, Marchesini M, et al. Oncogene ablation-resistant pancreatic cancer cells depend on mitochondrial function. Nature 2014;514:628–32.
6. Ying H, Kimmelman AC, Lyssiotis CA, Hua S, Chu GC, Fletcher-Sananikone E, et al. Oncogenic Kras maintains pancreatic tumors through regulation of anabolic glucose metabolism. Cell 2012;149:656–70.
7. Collins MA, Bednar F, Zhang Y, Brisset J-C, Galbán S, Galbán CJ, et al. Oncogenic Kras is required for both the initiation and maintenance of pancreatic cancer in mice. J Clin Invest 2012;122:639–53.
8. Ostrem JM, Peters U, Sos ML, Wells JA, Shokat KM. K-Ras(G12C) inhibitors allosterically control GTP affinity and effector interactions. Nature 2013;503:548–51.
9. Hallin J, Engstrom LD, Hargis L, Calinisan A, Aranda R, Briere DM, et al. The KRAS^{G12C} inhibitor MRTX849 provides insight toward therapeutic susceptibility of KRAS-mutant cancers in mouse models and patients. Cancer Discov 2020;10:54–71.
10. Canon J, Rex K, Saiki AY, Mohr C, Cooke K, Bagal D, et al. The clinical KRAS(G12C) inhibitor AMG 510 drives anti-tumour immunity. Nature 2019;575:217–23.
11. Hong DS, Fakih MG, Strickler JH, Desai J, Durm GA, Shapiro GI, et al. KRAS^{G12C} inhibition with sotorasib in advanced solid tumors. N Engl J Med 2020;383:1207–17.
12. Riely GJ, Ou S-HI, Rybkin I, Spira A, Papadopoulos K, Sabari JK, et al. 99O_PR KRYSTAL-1: activity and preliminary pharmacodynamic (PD) analysis of adagrasib (MRTX849) in patients (Pts) with advanced non–small cell lung cancer (NSCLC) harboring KRASG12C mutation. J Thoracic Oncol 2021;16:S751–2.
13. Jänne PA, Rybkin II, Spira AI, Riely GJ, Papadopoulos KP, Sabari JK, et al. KRYSTAL-1: activity and safety of adagrasib (MRTX849) in advanced/ metastatic non–small-cell lung cancer (NSCLC) harboring KRAS^{G12C} mutation. Eur J Cancer 2020;138(Suppl 2):S1–2.
14. Sacher A, LoRusso P, Patel MR, Miller WH Jr, Garralda E, Forster MD, et al. Single-agent divarasib (GDC-6036) in solid tumors with a KRAS G12C mutation. N Engl J Med 2023;389:710–21.
15. de Langen AJ, Johnson ML, Mazieres J, Dingemans A-MC, Mountzios G, Pless M, et al. Sotorasib versus docetaxel for previously treated non-small-cell lung cancer with KRAS^{G12C} mutation: a randomised, open-label, phase 3 trial. Lancet 2023;401:733–46.
16. Schulze CJ, Seamon KJ, Zhao Y, Yang YC, Cregg J, Kim D, et al. Chemical remodeling of a cellular chaperone to target the active state of mutant KRAS. Science 2023;381:794–9.
17. Weiss A, Lorthiois E, Barys L, Beyer KS, Bomio-Confaglia C, Burks H, et al. Discovery, preclinical characterization, and early clinical activity of JDQ443, a structurally novel, potent, and selective covalent oral inhibitor of KRASG12C. Cancer Discov 2022;12:1500–17.
18. Awad MM, Liu S, Rybkin II, Arbour KC, Dilly J, Zhu VW, et al. Acquired resistance to KRAS^{G12C} inhibition in cancer. N Engl J Med 2021;384:2382–93.
19. Zhao Y, Murciano-Goroff YR, Xue JY, Ang A, Lucas J, Mai TT, et al. Diverse alterations associated with resistance to KRAS(G12C) inhibition. Nature 2021;599:679–83.
20. Tanaka N, Lin JJ, Li C, Ryan MB, Zhang J, Kiedrowski LA, et al. Clinical acquired resistance to KRAS^{G12C} inhibition through a novel KRAS switch-II pocket mutation and polyclonal alterations converging on RAS-MAPK reactivation. Cancer Discov 2021;11:1913–22.
21. Ryan MB, Fece De La Cruz F, Phat S, Myers DT, Wong E, Shahzade HA, et al. Vertical pathway inhibition overcomes adaptive feedback resistance to KRAS^{G12C} inhibition. Clin Cancer Res 2020;26:1633–43.
22. Xue JY, Zhao Y, Aronowitz J, Mai TT, Vides A, Qeriqi B, et al. Rapid non-uniform adaptation to conformation-specific KRAS(G12C) inhibition. Nature 2020;577:421–5.
23. Tong X, Patel AS, Kim E, Li H, Chen Y, Li S, et al. Adeno-to-squamous transition drives resistance to KRAS inhibition in LKB1 mutant lung cancer. Cancer Cell 2024:42;413–28.e7.
24. Tsai YS, Woodcock MG, Azam SH, Thorne LB, Kanchi KL, Parker JS, et al. Rapid idiosyncratic mechanisms of clinical resistance to KRAS G12C inhibition. J Clin Invest 2022;132:e155523.
25. Lee JK, Sivakumar S, Schrock AB, Madison R, Fabrizio D, Gjoerup O, et al. Comprehensive pan-cancer genomic landscape of KRAS altered cancers and real-world outcomes in solid tumors. NPJ Precis Oncol 2022;6:91.
26. Strickler JH, Satake H, George TJ, Yaeger R, Hollebecque A, Garrido-Laguna I, et al. Sotorasib in KRAS p.G12C–mutated advanced pancreatic cancer. N Engl J Med 2023;388:33–43.
27. Bekaii-Saab TS, Yaeger R, Spira AI, Pelster MS, Sabari JK, Hafez N, et al. Adagrasib in advanced solid tumors harboring a KRAS^{G12C} mutation. J Clin Oncol 2023;41:4097–106.
28. Wang-Gillam A, Hubner RA, Siveke JT, Von Hoff DD, Belanger B, de Jong FA, et al. NAPOLI-1 phase 3 study of liposomal irinotecan in metastatic pancreatic cancer: final overall survival analysis and characteristics of long-term survivors. Eur J Cancer 2019;108:78–87.
29. Huffman BM, Basu Mallick A, Horick NK, Wang-Gillam A, Hosein PJ, Morse MA, et al. Effect of a MUC5AC antibody (NPC-1C) administered with second-line gemcitabine and nab-paclitaxel on the survival of patients with advanced pancreatic ductal adenocarcinoma: a randomized clinical trial. JAMA Netw Open 2023;6:e2249720.
30. Hallin J, Bowcut V, Calinisan A, Briere DM, Hargis L, Engstrom LD, et al. Anti-tumor efficacy of a potent and selective non-covalent KRAS^{G12D} inhibitor. Nat Med 2022;28:2171–82.

31. Wang X, Allen S, Blake JF, Bowcut V, Briere DM, Calinisan A, et al. Identification of MRTX1133, a noncovalent, potent, and selective KRAS^{G12D} inhibitor. J Med Chem 2022;65:3123–33.
32. Mahadevan KK, McAndrews KM, LeBleu VS, Yang S, Lyu H, Li B, et al. KRAS^{G12D} inhibition reprograms the microenvironment of early and advanced pancreatic cancer to promote FAS-mediated killing by CD8^{+} T cells. Cancer Cell 2023;41:1606–20.e8.
33. Kemp SB, Cheng N, Markosyan N, Sor R, Kim I-K, Hallin J, et al. Efficacy of a small-molecule inhibitor of KrasG12D in immunocompetent models of pancreatic cancer. Cancer Discov 2023;13:298–311.
34. Gulay KCM, Zhang X, Pantazopoulou V, Patel J, Esparza E, Pran Babu DS, et al. Dual inhibition of KRASG12D and pan-ERBB is synergistic in pancreatic ductal adenocarcinoma. Cancer Res 2023;83:3001–12.
35. Shao DD, Xue W, Krall EB, Bhutkar A, Piccioni F, Wang X, et al. KRAS and YAP1 converge to regulate EMT and tumor survival. Cell 2014;158:171–84.
36. Kapoor A, Yao W, Ying H, Hua S, Liewen A, Wang Q, et al. Yap1 activation enables bypass of oncogenic Kras addiction in pancreatic cancer. Cell 2014;158:185–97.
37. Singh A, Greninger P, Rhodes D, Koopman L, Violette S, Bardeesy N, et al. A gene expression signature associated with "K-Ras addiction" reveals regulators of EMT and tumor cell survival. Cancer Cell 2009;15:489–500.
38. Genovese G, Carugo A, Tepper J, Robinson FS, Li L, Svelto M, et al. Synthetic vulnerabilities of mesenchymal subpopulations in pancreatic cancer. Nature 2017;542:362–6.
39. Hou P, Kapoor A, Zhang Q, Li J, Wu C-J, Li J, et al. Tumor microenvironment remodeling enables bypass of oncogenic KRAS dependency in pancreatic cancer. Cancer Discov 2020;10:1058–77.
40. Hou P, Ma X, Yang Z, Zhang Q, Wu C-J, Li J, et al. USP21 deubiquitinase elevates macropinocytosis to enable oncogenic KRAS bypass in pancreatic cancer. Genes Dev 2021;35:1327–32.
41. Bahrambeigi V, Lee JJ, Branchi V, Rajapakshe KI, Xu Z, Kui N, et al. Transcriptomic profiling of plasma extracellular vesicles enables reliable annotation of the cancer-specific transcriptome and molecular subtype. Cancer Res 2024;84:1719–32.
42. Yu C, Mannan AM, Yvone GM, Ross KN, Zhang Y-L, Marton MA, et al. High-throughput identification of genotype-specific cancer vulnerabilities in mixtures of barcoded tumor cell lines. Nat Biotechnol 2016;34:419–23.
43. Corsello SM, Nagari RT, Spangler RD, Rossen J, Kocak M, Bryan JG, et al. Discovering the anticancer potential of non-oncology drugs by systematic viability profiling. Nat Cancer 2020;1:235–48.
44. Raghavan S, Winter PS, Navia AW, Williams HL, DenAdel A, Lowder KE, et al. Microenvironment drives cell state, plasticity, and drug response in pancreatic cancer. Cell 2021;184:6119–37.e26.
45. Krall EB, Wang B, Munoz DM, Ilic N, Raghavan S, Niederst MJ, et al. KEAP1 loss modulates sensitivity to kinase targeted therapy in lung cancer. Elife 2017;6:e18970.
46. Burke JE, Perisic O, Masson GR, Vadas O, Williams RL. Oncogenic mutations mimic and enhance dynamic events in the natural activation of phosphoinositide 3-kinase p110α (PIK3CA). Proc Natl Acad Sci U S A 2012;109:15259–64.
47. Orloff MS, He X, Peterson C, Chen F, Chen J-L, Mester JL, et al. Germline PIK3CA and AKT1 mutations in cowden and cowden-like syndromes. Am J Hum Genet 2013;92:76–80.
48. Cancer Genome Atlas Research Network. Integrated genomic characterization of pancreatic ductal adenocarcinoma. Cancer Cell 2017;32:185–203.e13.
49. Hingorani SR, Wang L, Multani AS, Combs C, Deramaudt TB, Hruban RH, et al. Trp53R172H and KrasG12D cooperate to promote chromosomal instability and widely metastatic pancreatic ductal adenocarcinoma in mice. Cancer Cell 2005;7:469–83.
50. Gavish A, Tyler M, Greenwald AC, Hoefflin R, Simkin D, Tschernichovsky R, et al. Hallmarks of transcriptional intratumour heterogeneity across a thousand tumours. Nature 2023;618:598–606.
51. Kinker GS, Greenwald AC, Tal R, Orlova Z, Cuoco MS, McFarland JM, et al. Pan-cancer single-cell RNA-seq identifies recurring programs of cellular heterogeneity. Nat Genet 2020;52:1208–18.
52. Hwang WL, Jagadeesh KA, Guo JA, Hoffman HI, Yadollahpour P, Reeves JW, et al. Single-nucleus and spatial transcriptome profiling of pancreatic cancer identifies multicellular dynamics associated with neoadjuvant treatment. Nat Genet 2022;54:1178–91.
53. Barkley D, Moncada R, Pour M, Liberman DA, Dryg I, Werba G, et al. Cancer cell states recur across tumor types and form specific interactions with the tumor microenvironment. Nat Genet 2022;54:1192–201.
54. Levine JH, Simonds EF, Bendall SC, Davis KL, Amir El-AD, Tadmor MD, et al. Data-driven phenotypic dissection of AML reveals progenitor-like cells that correlate with prognosis. Cell 2015;162:184–97.
55. De Raedt T, Walton Z, Yecies JL, Li D, Chen Y, Malone CF, et al. Exploiting cancer cell vulnerabilities to develop a combination therapy for ras-driven tumors. Cancer Cell 2011;20:400–13.
56. Garcia PL, Miller AL, Yoon KJ. Patient-derived xenograft models of pancreatic cancer: overview and comparison with other types of models. Cancers (Basel) 2020;12:1327.
57. Chan-Seng-Yue M, Kim JC, Wilson GW, Ng K, Figueroa EF, O'Kane GM, et al. Transcription phenotypes of pancreatic cancer are driven by genomic events during tumor evolution. Nat Genet 2020;52:231–40.
58. Aung KL, Fischer SE, Denroche RE, Jang G-H, Dodd A, Creighton S, et al. Genomics-driven precision medicine for advanced pancreatic cancer: early results from the COMPASS trial. Clin Cancer Res 2018;24:1344–54.
59. O'Kane GM, Grünwald BT, Jang G-H, Masoomian M, Picardo S, Grant RC, et al. GATA6 expression distinguishes classical and basal-like subtypes in advanced pancreatic cancer. Clin Cancer Res 2020;26:4901–10.
60. Qiang L, Hoffman MT, Ali LR, Castillo JI, Kageler L, Temesgen A, et al. Transforming growth factor-β blockade in pancreatic cancer enhances sensitivity to combination chemotherapy. Gastroenterology 2023;165:874–90.e10.
61. Pylayeva-Gupta Y, Lee KE, Hajdu CH, Miller G, Bar-Sagi D. Oncogenic Kras-induced GM-CSF production promotes the development of pancreatic neoplasia. Cancer Cell 2012;21:836–47.
62. Bayne LJ, Beatty GL, Jhala N, Clark CE, Rhim AD, Stanger BZ, et al. Tumor-derived granulocyte-macrophage colony-stimulating factor regulates myeloid inflammation and T cell immunity in pancreatic cancer. Cancer Cell 2012;21:822–35.
63. Amodio V, Yaeger R, Arcella P, Cancelliere C, Lamba S, Lorenzato A, et al. EGFR blockade reverts resistance to KRAS^{G12C} inhibition in colorectal cancer. Cancer Discov 2020;10:1129–39.
64. Qi C, Gong J, Li J, Liu D, Qin Y, Ge S, et al. Claudin18.2-specific CAR T cells in gastrointestinal cancers: phase 1 trial interim results. Nat Med 2022;28:1189–98.
65. Shah MA, Shitara K, Ajani JA, Bang Y-J, Enzinger P, Ilson D, et al. Zolbetuximab plus CAPOX in CLDN18.2-positive gastric or gastroesophageal junction adenocarcinoma: the randomized, phase 3 GLOW trial. Nat Med 2023;29:2133–41.
66. Chen J, Xu Z, Hu C, Zhang S, Zi M, Yuan L, et al. Targeting CLDN18.2 in cancers of the gastrointestinal tract: new drugs and new indications. Front Oncol 2023;13:1132319.
67. Lengrand J, Pastushenko I, Vanuytven S, Song Y, Venet D, Sarate RM, et al. Pharmacological targeting of netrin-1 inhibits EMT in cancer. Nature 2023;620:402–8.
68. Cassier PA, Navaridas R, Bellina M, Rama N, Ducarouge B, Hernandez-Vargas H, et al. Netrin-1 blockade inhibits tumour growth and EMT features in endometrial cancer. Nature 2023;620:409–16.
69. Nilsson MB, Yang Y, Heeke S, Patel SA, Poteete A, Udagawa H, et al. CD70 is a therapeutic target upregulated in EMT-associated EGFR tyrosine kinase inhibitor resistance. Cancer Cell 2023;41:340–55.e6.
70. Mugarza E, van Maldegem F, Boumelha J, Moore C, Rana S, Llorian Sopena M, et al. Therapeutic KRAS^{G12C} inhibition drives effective interferon-mediated antitumor immunity in immunogenic lung cancers. Sci Adv 2022;8:eabm8780.
71. Kim D, Herdeis L, Rudolph D, Zhao Y, Böttcher J, Vides A, et al. Pan-KRAS inhibitor disables oncogenic signalling and tumour growth. Nature 2023;619:160–6.

72. Jiang J, Jiang L, Maldonato BJ, Wang Y, Holderfield M, Aronchik I, et al. Translational and therapeutic evaluation of RAS-GTP inhibition by RMC-6236 in RAS-driven cancers. Cancer Discov 2024;14:994–1017.
73. Holderfield M, Lee BJ, Jiang J, Tomlinson A, Seamon KJ, Mira A, et al. Concurrent inhibition of oncogenic and wild-type RAS-GTP for cancer therapy. Nature 2024;629:919–26.
74. Wasko UN, Jiang J, Dalton TC, Curiel-Garcia A, Edwards AC, Wang Y, et al. Tumour-selective activity of RAS-GTP inhibition in pancreatic cancer. Nature 2024;629:927–36
75. Eisenhauer EA, Therasse P, Bogaerts J, Schwartz LH, Sargent D, Ford R, et al. New response evaluation criteria in solid tumours: revised RECIST guideline (version 1.1). Eur J Cancer 2009;45:228–47.
76. Raymond CK, Hernandez J, Karr R, Hill K, Li M. Collection of cell-free DNA for genomic analysis of solid tumors in a clinical laboratory setting. PLoS One 2017;12:e0176241.
77. Steen CB, Liu CL, Alizadeh AA, Newman AM. Profiling cell type abundance and expression in bulk tissues with CIBERSORTx. Methods Mol Biol 2020;2117:135–57.
78. Wang K, Patkar S, Lee JS, Gertz EM, Robinson W, Schischlik F, et al. Deconvolving clinically relevant cellular immune cross-talk from bulk gene expression using CODEFACS and LIRICS stratifies patients with melanoma to anti-PD-1 therapy. Cancer Discov 2022;12:1088–105.
79. Love MI, Huber W, Anders S. Moderated estimation of fold change and dispersion for RNA-seq data with DESeq2. Genome Biol 2014;15:550.
80. Garcia EP, Minkovsky A, Jia Y, Ducar MD, Shivdasani P, Gong X, et al. Validation of OncoPanel: a targeted next-generation sequencing assay for the detection of somatic variants in cancer. Arch Pathol Lab Med 2017;141:751–8.
81. Li J, Byrne KT, Yan F, Yamazoe T, Chen Z, Baslan T, et al. Tumor cell-intrinsic factors underlie heterogeneity of immune cell infiltration and response to immunotherapy. Immunity 2018;49:178–93.e7.
82. Ianevski A, Giri AK, Aittokallio T. SynergyFinder 3.0: an interactive analysis and consensus interpretation of multi-drug synergies across multiple samples. Nucleic Acids Res 2022;50:W739–43.
83. Schindelin J, Arganda-Carreras I, Frise E, Kaynig V, Longair M, Pietzsch T, et al. Fiji: an open-source platform for biological-image analysis. Nat Methods 2012;9:676–82.
84. Carugo A, Genovese G, Seth S, Nezi L, Rose JL, Bossi D, et al. In vivo functional platform targeting patient-derived xenografts identifies WDR5-myc association as a critical determinant of pancreatic cancer. Cell Rep 2016;16:133–47.
85. Bankhead P, Loughrey MB, Fernández JA, Dombrowski Y, McArt DG, Dunne PD, et al. QuPath: open source software for digital pathology image analysis. Sci Rep 2017;7:16878.
86. Williams HL, Dias Costa A, Zhang J, Raghavan S, Winter PS, Kapner KS, et al. Spatially resolved single-cell assessment of pancreatic cancer expression subtypes reveals co-expressor phenotypes and extensive intratumoral heterogeneity. Cancer Res 2023;83:441–55.
87. Stephens M. False discovery rates: a new deal. Biostatistics 2017;18:275–94.
88. Moffitt RA, Marayati R, Flate EL, Volmar KE, Loeza SGH, Hoadley KA, et al. Virtual microdissection identifies distinct tumor- and stroma-specific subtypes of pancreatic ductal adenocarcinoma. Nat Genet 2015;47:1168–78.
89. Pitter KL, Grbovic-Huezo O, Joost S, Singhal A, Blum M, Wu K, et al. Systematic comparison of pancreatic ductal adenocarcinoma models identifies a conserved highly plastic basal cell state. Cancer Res 2022;82:3549–60.
90. Collisson EA, Sadanandam A, Olson P, Gibb WJ, Truitt M, Gu S, et al. Subtypes of pancreatic ductal adenocarcinoma and their differing responses to therapy. Nat Med 2011;17:500–3.
91. Bailey P, Chang DK, Nones K, Johns AL, Patch A-M, Gingras M-C, et al. Genomic analyses identify molecular subtypes of pancreatic cancer. Nature 2016;531:47–52.